國立臺灣大學工學院材料科學與工程學研究所

碩士論文

Department of Materials Science and Engineering
College of Engineering
National Taiwan University

Master Thesis

探索帶電之官能化聚(3,4-乙烯基二氧噻吩)共聚物及兩性離子高分子刷在抗生物沾黏上之應用

Explore the Antifouling Applications in Charged Functionalized Poly(3,4-ethylenedioxythiophene) Copolymer and Zwitterionic Polymer Brush

林姿妤

Tzu-Yu Lin

指導教授：羅世強 博士

Advisor: Shyh-Chyang Luo, Ph.D.

中華民國 112 年 7 月

July, 2023

doi:10.6342/NTU202301269

致謝

能夠順利完成這篇論文要感謝的人很多，其中對我幫助最多的一位那必須要提到我的指導教授羅世強老師。從大學專題到繼續留在羅 lab 讀碩士，這一步一步走來，在研究方面羅老師給予了我足夠的自由，在研究方向的選擇方面非常尊重我選擇自己感興趣的題目，並且在各方面支持我追逐自己想要的。在生活方面，羅老師也無疑是最佳心靈導師，老師每次見到我最常問的一句話就是最近過得怎麼樣，很普通平凡的一句關心卻往往是最溫暖的問候。並且自從我大學時期跟老師說過我想要出國讀書之後，老師也是一步步為我規劃，讓我能夠順利發表一篇文章來豐富自己的履歷，申請失利之後老師也提出了各種方案想要幫助我做自己想做的事，真的特別感動也特別感謝。

另外我也要特別感謝康敦彥老師以及康老師實驗室的同學，在我完全沒接觸過也不熟悉的領域給予我很多研究上的幫助，也很細心地回答我各種問題，雖然在康老師實驗室待的時間很短，但還是收穫了滿滿的善意與幫助。

最後的最後，我也要真誠的感謝羅 lab 的每一位學長姐和同學，謝謝大家陪我討論實驗數據，為我答疑解惑，我愛羅實驗室真的是一間非常溫馨的實驗室，謝謝大家。

doi:10.6342/NTU202301269

中文摘要

隨著醫療技術的進步，生物醫學應用相關的研究也大幅增加。在不同的材料中，聚(3,4-乙二氧基噻吩)（PEDOT）被認為是一種有潛力的導電材料，可用於生物電子傳感器。為了研究 PEDOT 表面電荷對蛋白質結合行為的影響，我們開發了一種新的帶正電荷的官能化 EDOT 單體，即 EDOT-N^+。我們使用電化學方法將帶有負電荷的羧酸官能化 EDOT 單體（EDOT-COOH）與 EDOT-N^+進行共聚，並調整了不同的單體比例。結果表明，在 [EDOT-N^+] : [EDOT-COOH] = 8:2 的比例下，實際鍍上去的高分子共聚物的比例會是 1:1，此 poly(EDOT-N^+-*co*-EDOT-COOH)共聚物表現出良好的抗污染性能。因此，我們提出了一種由等密度正負官能基團組成的共聚物產生類似兩性離子高分子的抗污染性能。

除了在生物醫學領域的應用外，兩性離子高分子的特殊抗污染性能使其在許多不同的領域中同樣成為受歡迎的材料。隨著水資源短缺的問題日益嚴重，新型淨水技術的研發變得刻不容緩。太陽能水純化被認為是一種有前景的方法，因為地球表面有 71%的面積被水覆蓋，其中蘊藏量最大的就是海水，再加上隨處可得源源不絕的太陽能可供利用，這將會是一種環境友善且永續的淨水方式。我們設計了一個雙層結構的太陽能水純化平台，利用吸水性良好的醋酸纖維膜作為基材，配合金屬有機框架作為絕緣層，同時利用其多孔結構進行水傳輸。碳黑和聚多巴胺則是作為吸光材，將吸收的光轉化為熱能。而為了延長太陽能水純化平台的使用壽命，我

doi:10.6342/NTU202301269

們特別在平台底部設計了一層兩性離子高分子刷旨在實現抗污染功能，使水中的污染物不會沾附在平台上，以防止平台的多孔結構被堵塞而導致水純化效率下降甚至是失去功能。

關鍵字：表面電荷、兩性離子、抗污染表面、石英晶體微量天平、電聚合、官能化聚(3,4-乙二氧基噻吩)（EDOT）、太陽能水純化、金屬有機框架、兩性離子高分子刷、水蒸發

doi:10.6342/NTU202301269

ABSTRACT

With the advancement of medical technology, research in biomedical applications also essentially increases. Among different materials, poly(3,4-ethylenedioxythiophene) (PEDOT) has been regarded as a promising conductive material for bioelectronics. To investigate the surface charge effect on protein binding behavior on PEDOT, we developed a new positively charged functionalized EDOT monomer, EDOT-N^+. We used an electrochemical method to copolymerize EDOT-N^+ with negatively charged carboxylic acid-functionalized EDOT monomer, EDOT-COOH, with different feed ratios. The results show that at [EDOT- N^+] : [EDOT-COOH] = 8:2, where an actual 1:1 ratio of the copolymer was determined, the poly(EDOT-N^+-*co*-EDOT-COOH) presented good antifouling performance. Therefore, we propose a zwitterion-like antifouling property from the poly(EDOT-N^+-*co*-EDOT-COOH) with an equal density of both positive and negative functional groups.

Despite applications in the biomedical field, the special antifouling property of zwitterionic polymer makes it a popular material in many different professions. As the water scarcity issue becomes more serious, there must come out with some solutions to produce clean water. Solar desalination has been regarded as a promising method since there is inexhaustible seawater on earth and ubiquitous solar energy readily available.

doi:10.6342/NTU202301269

This would be an environmental-friendly and sustainable method to produce clean water. We designed a double-layer structure for the desalination platform with a highly water-sorbent cellulose acetate membrane as the substrate and metal-organic framework working as the insulating layer while also serving as water absorbing layer crediting to the porous structure to allow water transport. Carbon black and polydopamine are solar-absorbing materials that convert absorbed light into heat. To extend the service life of the platform, we especially designed a layer of zwitterionic polymer brush at the bottom of the desalination platform aiming to provide an antifouling function so that the pollutants in the water would be repelled from the platform, preventing the porous structure of the platform being obstructed and make the platform fail.

KEYWORDS: Surface charge, zwitterion, antifouling surface, quartz crystal microbalance, electropolymerization, functionalized-EDOT, solar desalination, metal-organic framework, zwitterionic polymer brush, water evaporation

doi:10.6342/NTU202301269

CONTENTS

doi:10.6342/NTU202301269

doi:10.6342/NTU202301269

doi:10.6342/NTU202301269

doi:10.6342/NTU202301269

doi:10.6342/NTU202301269

LIST OF FIGURES

doi:10.6342/NTU202301269

doi:10.6342/NTU202301269

doi:10.6342/NTU202301269

doi:10.6342/NTU202301269

doi:10.6342/NTU202301269

doi:10.6342/NTU202301269

doi:10.6342/NTU202301269

LIST OF TABLES

doi:10.6342/NTU202301269

Chapter 1 Introduction

1.1 Conducting Polymer in Biomedical Applications

1.1.1 Antifouling Conducting Polymer

Apart from the conventional understanding that polymers are insulating materials, conducting polymers (CPs), π-conjugated polymers[1] with backbones made up of repeating alternating single and double bonds are a class of materials with high electrical conductivity and have unique mechanical and optical properties. In recent years, conducting polymers (CPs) have also attracted much attention in biomedical applications for their tissue-like softness, high chemical stability, biocompatibility, and low-cost fabrication.[2-5] Biomedical research of CPs has been widely explored in biosensors, tissue engineering, drug delivery, etc.[6-9] More recently, the focus of CP application has shifted to the implanted devices,[10, 11] including the bioelectrodes and bioelectronics.[12, 13]. The coating of CPs, especially PEDOT-based material, outperformed due to its low impedance property,[14-17] allowing efficient charge transfer at the surface. Moreover, it can also help to reduce signal-to-noise ratio[18] to promote sensitivity of the device, and the increase of charge injection[19] effect also make PEDOT widely applicable in neural signal recording and stimulation. As for implanted devices, nonspecific protein adsorption or cell adhesion may cause an immune response and may obstruct the reactive site leading to malfunction of the device.[20] Thus, research on antifouling conducting polymers has become

doi:10.6342/NTU202301269

increasingly important. Varying the surface properties of the CPs by surface modifications[21] is critical to promoting the performance, such as lifetime and biocompatibility, of the CP-coated implanted devices.

In general, antifouling conducting polymers are mainly classified into two types,[22, 23] poly(ethylene glycol) (PEG) or oligo(ethylene glycol) (OEG)-based, and zwitterionic polymers,[24, 25] both comprised of neutral units. Various OEG-functionalized or zwitterion-functionalized CPs have been demonstrated.[26] Huang et al.[27] have recently presented that the increase in EG units of OEG-functionalized PEDOTs reduces the adhesion between the PEDOT and AFM tips and exhibits relatively few adhered platelets. Mukai et al.[28] have demonstrated conducting polymer with zwitterionic choline phosphate groups, which presents good antifouling properties and an unusual adhesive property to cells. Lin and Luo[29] also studied the nonspecific protein binding (BSA) and specific protein binding (CRP) behavior of poly(2-methacryloyloxyethyl phosphorylcholine) (PMPC)[30] and poly(sulfobetaine methacrylate) (PSBMA) polymer brushes[31, 32] under the influence of varying ion concentration and surface potential. The recent development in this field has been summarized in some review articles.[20, 33]

1.1.2 Zwitterionic Polymer

Among different kinds of antifouling conducting polymers, zwitterionic polymers especially have some special properties. Zwitterionic polymer is a kind of polymer

doi:10.6342/NTU202301269

composed of repeating units comprising equal amounts of opposite charges. The positive and negative charges of the zwitterionic moieties would induce dipole moment, leading to the alignment of water molecules along the zwitterionic molecules' dipole moment to form a cage-like structure (**Figure 1-1a**) around zwitterions known as a hydration shell. Ionic solvation attracts water molecules to the charged functional groups of the zwitterion, resulting in the formation of an energy barrier that biomolecules must overcome to make contact with the zwitterion, which is proposed to be the source of antifouling property of the zwitterionic molecules.[34]

In addition, since zwitterionic molecules have equal amounts of opposite charges on the repeating units, there was a special phenomenon called the anti-polyelectrolyte effect (**Figure 1-1b**). In general, charged polyelectrolytes in pure water would extend the polymer chain due to the electrostatic repulsion force between similar charges. When salt is added into the water, the electrostatic attraction between ions and charged polymer chains would cause the polymer chains to collapse. In contrast, zwitterionic polymers with equal amounts of charges on repeating units exhibit chain collapse due to electrostatic attraction within and between the polymer chains. The addition of salt can screen the electrostatic attraction between polymer chains, allowing the chains to extend and capture more water molecules, preventing protein adsorption.

doi:10.6342/NTU202301269

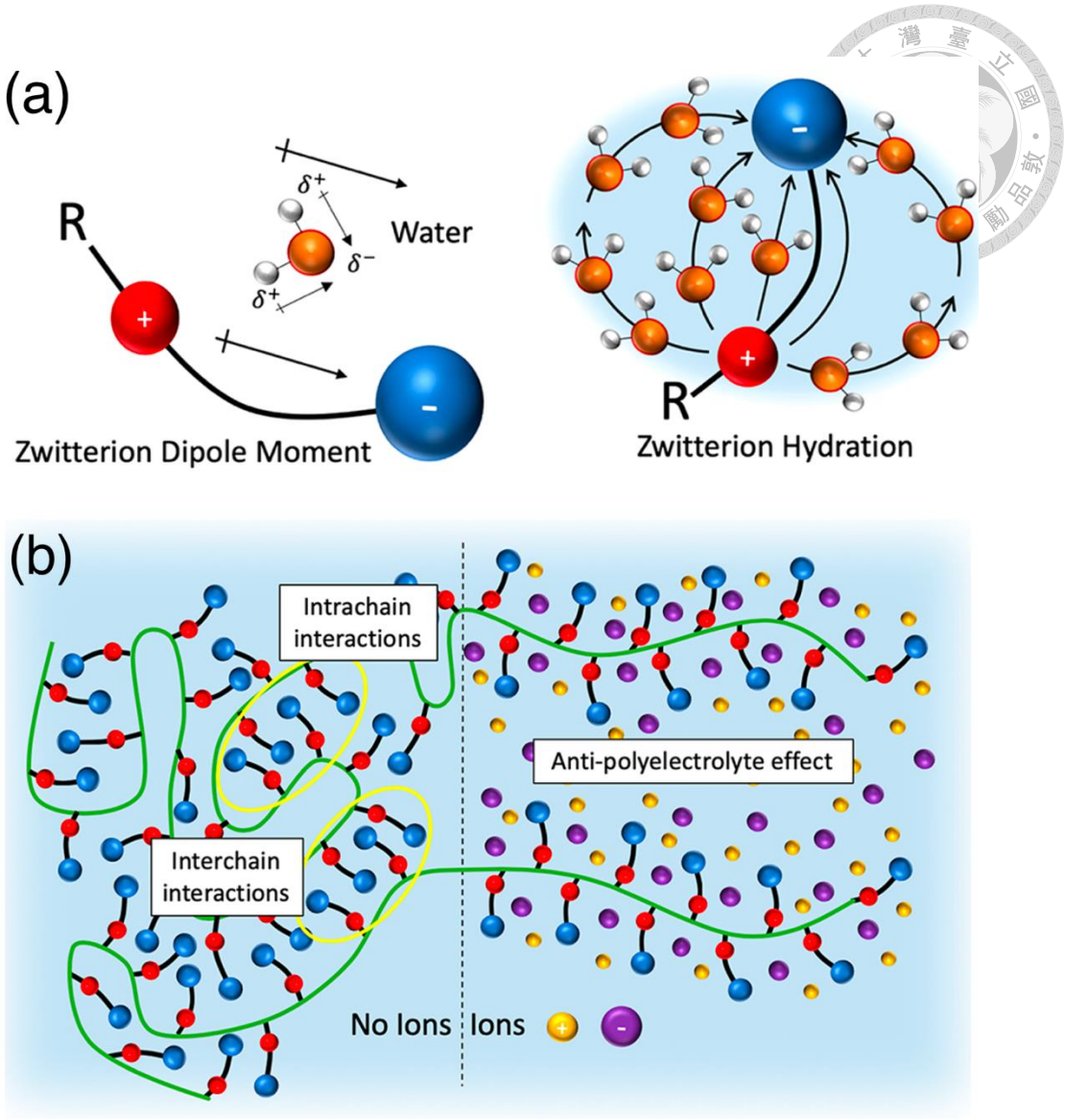

Figure 1-1. Schematic diagram of (a) the formation of cage-like hydration shell around zwitterionic moiety, (b) anti-polyelectrolyte effect on inter- and intra- chain interactions of zwitterionic polymer chains in the presence of ions.[34]

doi:10.6342/NTU202301269

1.2 Utilize Metal-Organic Framework and Polymer Brush Design in Solar Desalination System

Since the 1800s, human activities have been the main driver of climate change, leading to severe consequences worldwide, including water scarcity. Climate change has also largely influenced the weather in Taiwan: the unsteady rainfalls cause the water supply to become unstable. Using water purification technologies can expand the source of clean water to solve the problem of water deficit.

Solar steam generation[35-37] is considered a promising technique among various methods due to the clean, sustainable, and inexhaustible nature of solar energy. Additionally, considering that the ocean is the largest water body in the world, if we could make good use of this resource, seawater could also be a usable, easily available, and even drinkable water source. Combining these advantages presents a feasible method to utilize the abundant energy from the sun to heat seawater and generate steam, then condensing the steam to collect clean water, effectively removing salt and impurities. This approach offers a promising solution to address water scarcity in coastal or arid regions where access to freshwater sources is limited. By harnessing the power of the sun, water desalination can become an efficient, environmentally friendly way to offer a potential solution to the challenges of global water scarcity.

doi:10.6342/NTU202301269

1.2.1 Solar Desalination Platform

A solar water desalination device primarily relies on the photothermal membrane to convert absorbed solar energy into thermal energy. The mechanism[37, 38] of the desalination process is shown in **Figure 1-2**. The solid lines represent the energy transfer path that was actually utilized in the desalination process. Sunlight is absorbed by the surface, converted into heat, and then heats the water drawn from the bottom to the surface, causing it to evaporate. By collecting and condensing the steam, clean water can be obtained. The dashed lines represent the pathways for thermal energy leakage through thermal radiation, convection, and conduction. Therefore, based on the energy transfer route, we can conclude that there are two main approaches to improving solar water desalination efficiency: one is to increase the solar spectrum absorption range of the photothermal membrane to improve the light-to-heat conversion efficiency, and the other is to reduce thermal energy loss into the environment, thereby indirectly increasing thermal energy utilization.

doi:10.6342/NTU202301269

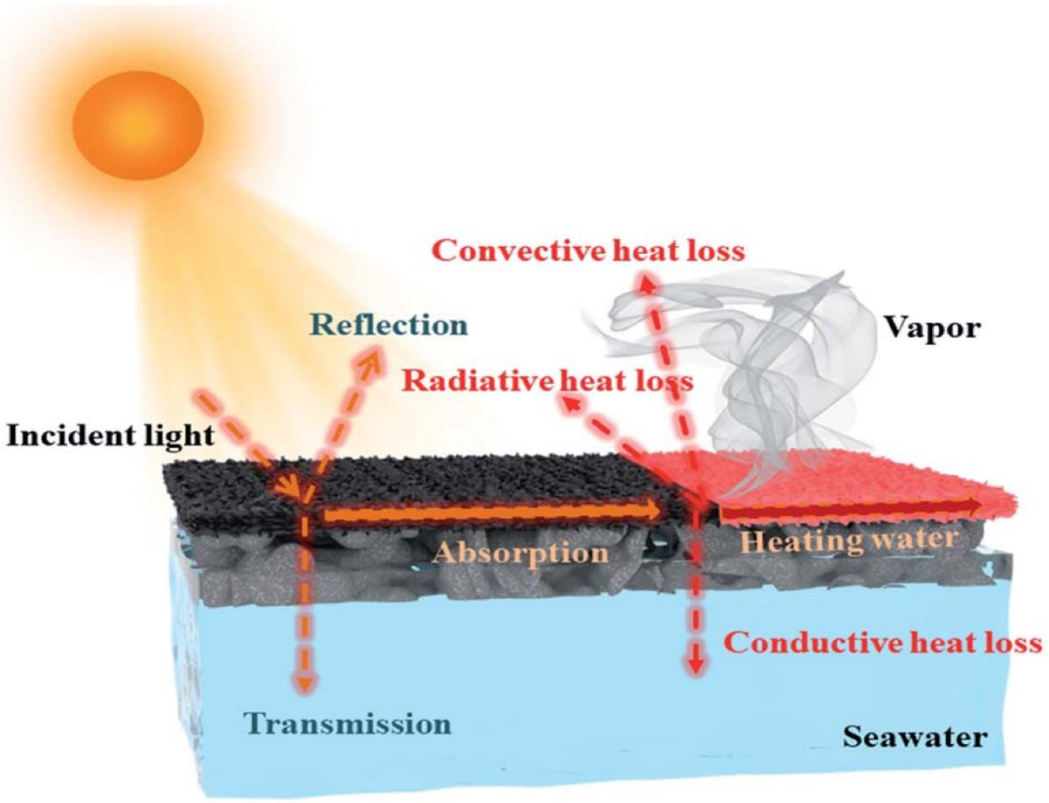

Figure 1-2. Schematic illustration of the solar-thermal interface desalination mechanism.[38]

1.2.2 Metal-Organic Framework in Desalination Platform

To minimize the energy loss, especially heat loss into the bulk water, a double-layer structure (**Figure 1-3b**) is designed with a layer of thermal insulator added directly below the photothermal layer to prevent heat loss to bulk water through conduction and concentrate heat on the top surface of the device. This insulating layer not only needs to have low thermal conductivity but also requires a strong capillary wicking ability to pump large amounts of water to the evaporation surface, which means the insulating membrane

doi:10.6342/NTU202301269

should possess pores with controllable size to improve water transport.

Metal-organic frameworks (MOFs)[39, 40] are organic and inorganic hybrid materials formed by coordinating transition metal ion centers with organic ligands, creating a crystalline structure with regular and tunable pores. The high porosity and controllable pore size allow water permeance, enabling MOF to function as a water-sucking layer. Abdullah et al.[41] have reasoned that small pore size and window cage would help to allow water transport while rejecting dissolved ions at the same time. Cao et al.[42] have also proved that over two layers of Ni/Cu-HAB MOF could reject almost 100% of ions and provide 3-6 orders of magnitude of water permeation rate compared to commercially used filtration materials through dynamic simulation, making it a promising material for water desalination. Additionally, the surface roughness of MOF prevents light reflection, and the low thermal conductivity helps the platform to concentrate heat on the surface. Hu et al.[43] had constructed an efficient metal-organic framework-based solar steam generation system using hydrophilic [Al(OH)(benzene-1,3-dicarboxylate)]·nH_2O (CAU-10-H) membrane as insulating layer which largely enhanced the surface temperature, reaching a high evaporation efficiency of 98%. Due to the porous structure with adjustable pore size and thermal insulating ability, MOFs have been utilized in solar desalination systems and serve as precursors for the photothermal layer.

doi:10.6342/NTU202301269

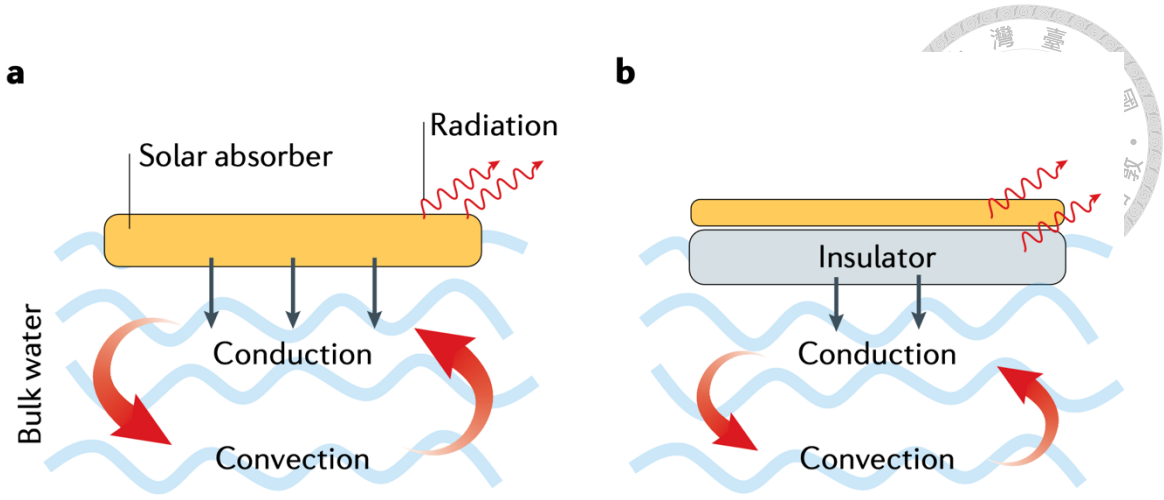

Figure 1-3. Figure. Schematic illustration of (a) single, (b) double layer floating solar steam generation device.[35]

1.2.3 Antifouling Zwitterionic Polymer Brush

As illustrated in the previous section, zwitterionic polymer possesses special antifouling properties due to the formation of a hydration layer on the surface, inhibiting protein adsorption. Moreover, due to the anti-polyelectrolyte effect, the zwitterionic polymer chain can expand in the presence of salt. As a result, the zwitterionic polymer is especially suitable to be utilized in solar desalination devices to be immersed in seawater. Various studies concerning zwitterion-modified platforms have been conducted. Liu et al.[44] have presented that the cellulose substrates modified with several kinds of zwitterionic polymer chains via surface-initiated atom transfer radical polymerization (SI-ATRP) method could significantly reduce the non-specific adsorption (**Figure 1-4**) of proteins, platelet adhesion, and cell attachment, presenting the good antifouling property.

doi:10.6342/NTU202301269

Xu et al.[45] also confirmed that the poly(N-isopropylacrylamide) (PNIPAm) hydrogel modified with poly(sulfobetaine methacrylate) (PSBMA) polymer brush could have good oil antifouling and self-cleaning capabilities (**Figure 1-5**).

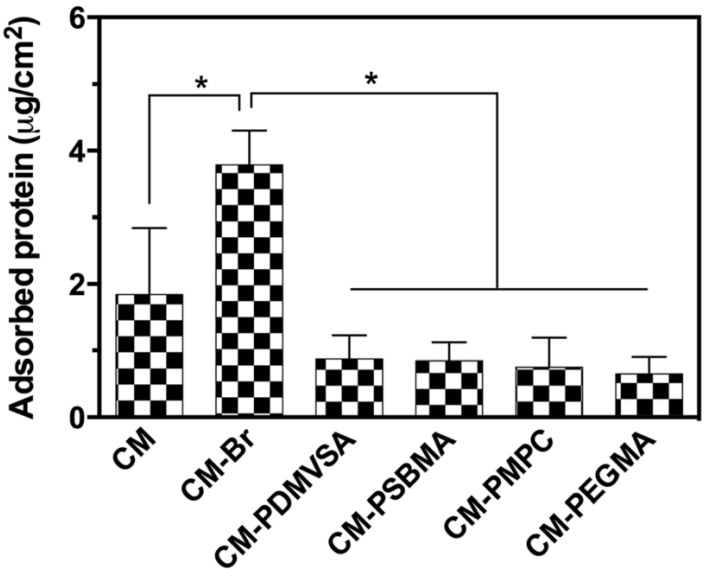

Figure 1-4. Protein adsorption on different cellulose membrane substrates. (*, $p < 0.05$)[44]

doi:10.6342/NTU202301269

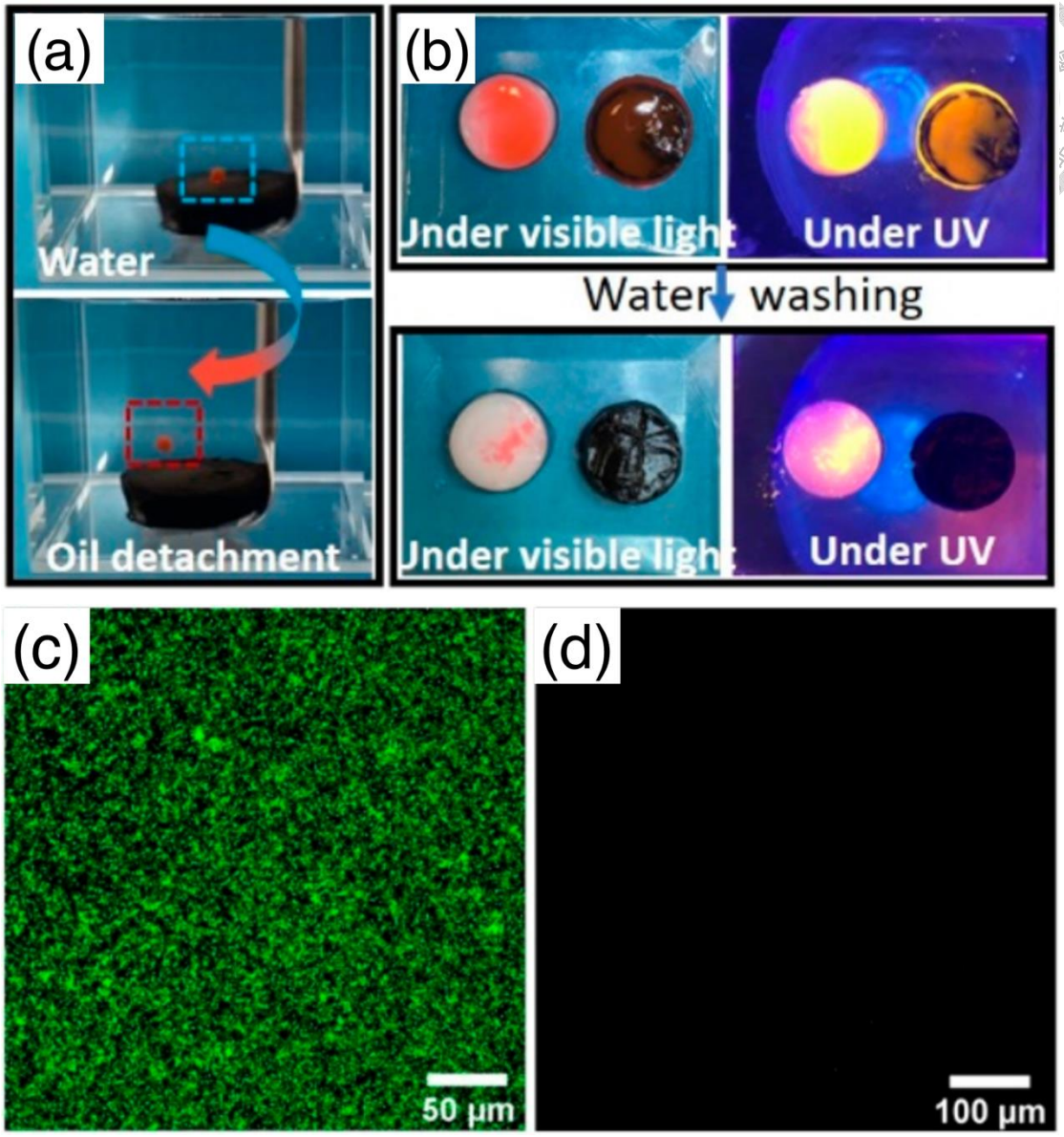

Figure 1-5. (a) Photographs of the Nile red labeled oil droplet fouling test. (b) Photographs of PNIPAm hydrogel with (black) and without (white) SBMA polymer brush taking Nile red labeled oil droplet fouling test. Fluorescence microscopy images of *E. coli* adsorption on (c) glass slide and (d) PNIPAm hydrogel with SBMA polymer brush.[45]

doi:10.6342/NTU202301269

1.3 Research Goal

1.3.1 Surface Charge Tuning of Poly(EDOT-N^+-*co*-EDOT-COOH)

According to previous experiences, surface charge plays a critical role in controlling the adsorption of proteins. For example, the positively charged surface attracts proteins with a net negative charge and repulses proteins with a net positive charge. Thus, out of our curiosity, if we synthesize a conducting polymer comprising both positively charged and negatively charged groups, could we expect to have a zwitterion-like antifouling property from this conducting polymer by tuning the amount of positively and negatively charged moieties to be neutral?

To prove this idea, in this study, we have synthesized a new positively charged EDOT monomer[46], EDOT-N^+, as shown in **Figure 1-6**. By mixing EDOT-N^+ and EDOT-COOH monomer solutions, we can prepare poly(EDOT-N^+-*co*-EDOT-COOH) by electropolymerization. The composition of poly(EDOT-N^+-*co*-EDOT-COOH) can be fine-tuned by changing the composition of monomer solutions. We then tested the adsorption of proteins on our poly(EDOT-N^+-*co*-EDOT-COOH) compared to poly(EDOT-N^+) and poly(EDOT-COOH). Two proteins, including bovine serum albumin (BSA) and lysozyme (LYZ), were used for the protein adsorption test. For a protein, the net charge is determined by its isoelectric point. BSA has an isoelectric point at approximately 4.9, indicating a net negative charge in a buffer solution at pH = 7.0.

doi:10.6342/NTU202301269

The isoelectric point of LYZ is about 10.7, meaning a net positive charge in a buffer solution at pH = 7.0. By comparing the adsorption behavior of both BSA and LYZ on poly(EDOT-N^+-*co*-EDOT-COOH) of different compositions, we would like to illustrate how the interactions between protein and polymer determine the protein adsorption behavior. Most importantly, by manipulating the surface charge of poly(EDOT-N^+-*co*-EDOT-COOH), we would like to examine the possibility of creating a zwitterion-like poly(EDOT-N^+-*co*-EDOT-COOH), which presents excellent antifouling properties. This work has been published on *Polymer* with the topic of "*Manipulating the Distribution of Surface Charge of PEDOT toward Zwitterion-Like Antifouling Properties*"[47] at 10 November, 2022. Some of the figures shown in the following sections would be captured from this article.

doi:10.6342/NTU202301269

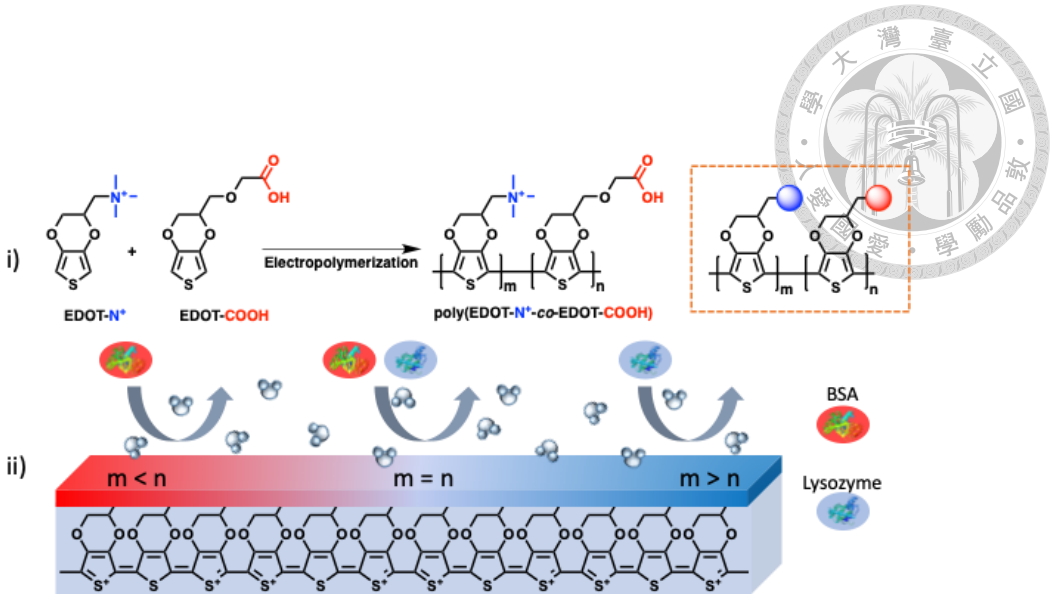

Figure 1-6. The scope of this study includes i) preparation of poly(EDOT-N$^+$-*co*-EDOT-COOH) thin films with tunable surface charges through electropolymerization, and ii) evaluation of antifouling properties of poly(EDOT-N$^+$-*co*-EDOT-COOH), m and n are the number of repeating units for EDOT-N$^+$ and EDOT-COOH respectively.[47]

1.3.2 Zwitterionic Polymer Brush-Modified Metal-Organic Framework-Based Solar Desalination Platform

According to previous researches,[48] the design of solar desalination system needs to meet the following four conditions as shown in **Figure 1-7**:

1. The light absorbing layer on the surface should be able to absorb a wide range of solar spectra and create a thermal zone on the surface under solar radiation.

2. The insulating layer material should have low thermal conductivity to suppress heat

doi:10.6342/NTU202301269

loss away from the thermal zone.

3. The structure's interior and bottom should have hydrophilic surfaces to utilize capillary force to facilitate upward water flow towards the thermal zone.

4. The structure's interior should have pores for water transport.

Based on these principles, we designed a double layer solar desalination platform with cellulose acetate (CA) membrane filter working as the substrate, then synthesizing a layer of CAU-10-H MOF layer as heat insulating material, and depositing the solar absorber layer made up of carbon black[49, 50] and polydopamine.[51, 52] The bottom of the CA substrate was modified with zwitterionic poly(sulfobetaine methacrylate) (PSBMA) polymer brush to enhance the antifouling property of the bottom of the platform so that contaminants and biomolecules in seawater would not block the porous structure and obstruct the water transport path.

doi:10.6342/NTU202301269

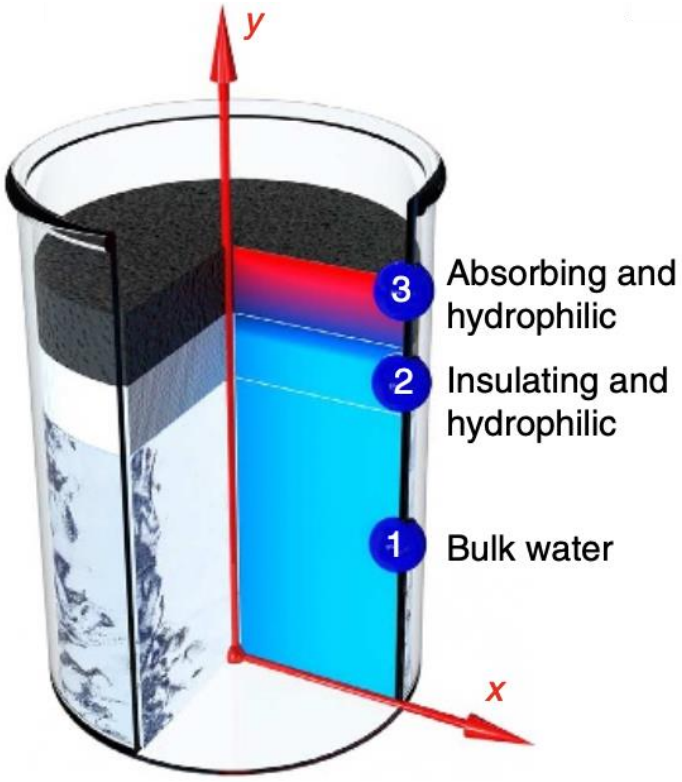

Figure 1-7. Schematic illustration of the cross section of the double-layer solar steam generation device showing the heat distribution.[48]

doi:10.6342/NTU202301269

Chapter 2 Materials and Methods

2.1 Materials and Instruments

2.1.1 Materials

Table 2-1. List of materials.

Supplier	Name	Purity
Sigma Aldrich	Bovine serum albumin (BSA)	96.0%
	Lysozyme (LYZ)	≥90.0%
	Phosphate-buffered saline (PBS) tablet	
	EDOT-OH monomer	
	Dopamine hydrochloride	
	2,2'-Bipyridyl reagent (Bpy)	≥99%
	Triethylamine	≥99.5%
	Tetrahydrofuran	≥99.9%
	Dichloromethane	
	[2-(Methacryloyloxy)ethyl]dimethyl-(3-sulfopropyl)ammonium hydroxide (SBMA)	95%

doi:10.6342/NTU202301269

ACROS	Sodium dodecyl sulfate (SDS)	
	Toluidine blue O (TBO)	
Alfa Aesar	Lithium perchlorate ($LiClO_4$)	
	Isophthalic acid	99%
	Copper(I) Bromide	
JT Baker	Aluminum sulfate octadecahydrate	
Macron	N,N-dimethylformamide (DMF)	99.8%
	Methanol	99%
TCI	2-Bromoisobutyryl bromide (BiBB)	>98%
	2-Dimethylaminopyridine	>98%

Table 2-2. List of membrane filters.

Supplier	Membrane	Pore Size
Finetech	Cellulose acetate	0.2 μm

doi:10.6342/NTU202301269

2.1.2 Instruments

Table 2-3. List of instruments.

Supplier	Instrument	Model
Biolin Scientific	Quartz Crystal Microbalance	Q-Sense E4
Autolab	Potentiostat	PGSTAT128N
Sindatek	Contact Angle Goniometer	Model 100SB
Bruker	Atomic Force Microscopy	Bioscope Resolve system
Shimadzu	UV-Vis Spectrophotometer	UV-1900i
JASCO	Fourier-transform Infrared Spectroscopy	FT/IR-6700typeA
Hitachi	Scanning Electron Microscope	S-4800
Rigaku	High-Power X-ray Diffractometer	Miniflex
Testo	Infrared camera	Testo 869
ULVAC-PHi	X-ray Photoelectron Spectroscope	PHI 5000 Versa Probe

doi:10.6342/NTU202301269

2.2 Fabrication of Poly(EDOT-N^+-*co*-EDOT-COOH) Film

2.2.1 Synthesis of EDOT-N^+ Monomer

EDOT-N^+ was synthesized according to previously reported method,[47] and the procedure is as shown in **Figure 2-1**. Following the tosylation of EDOT-OH, EDOT-OTs were subjected to an intermolecular nucleophilic substitution with trimethylamine, delivering EDOT-N^+ in excellent yield. For the synthesis of EDOT-OTs, a solution of EDOT-OH (300 mg, 1.74 mmol) in dry DCM (2.9 mL), 4-(dimethylamino)pyridine (0.004 g, 0.04 mmol), 4-toluenesulfonyl chloride (478 mg, 2.51 mmol), Et_3N (0.44 mL, 3.16 mmol) was added at 0℃ under N_2 atmosphere. The resulting mixture was stirred for 16 hours at room temperature. Then, the solution was diluted with ethyl acetate (10 mL) and then extracted with brine (5 mL, three times). The organic layer was dried over $MgSO_4$, filtered and concentrated. The crude product was purified by flash column chromatography (CH_2Cl_2:hexanes = 1:2) to obtain EDOT-OTs (349 mg, 61% yield) as light green solid (m.p. = 88-89 ℃). R_f : 0.40 (EtOAc:hexanes = 1:3). For the synthesis of EDOT-N^+, a solution of EDOT-OTs (0.323 g, 0.99 mmole) in acetonitrile (1.3 mL) was added trimethylamine (15 mL, 1.0 M in THF) at room temperature. The resulting mixture was transferred to a pressure tube and then stirred at 80 ℃ for 96 hours. After cooling to room temperature, the reaction mixture was concentrated under reduced pressure. Diethyl ether (20 mL) and DI water (20 mL) were sequentially added to the

doi:10.6342/NTU202301269

crude mixture (Note: The product is in the aqueous phase). Using a separatory funnel, the organic layer was separated and then washed with DI water (20 mL, six times). The combined aqueous layers were concentrated to obtain EDOT-N^+ (355 mg, 94% yield) as fawn solid (m.p. = 159-160 ℃).

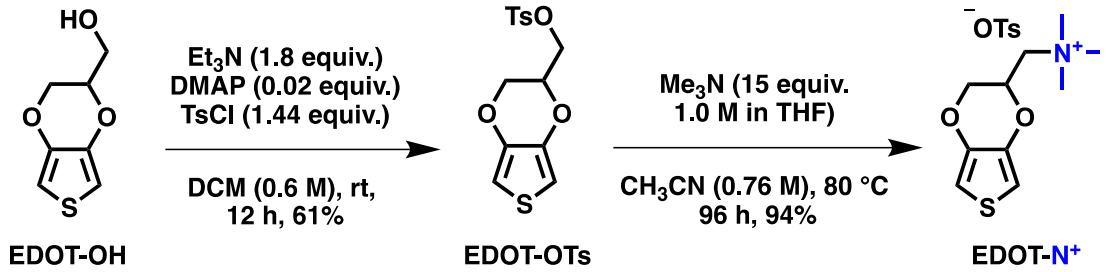

Figure 2-1. Schematic illustration of the synthesis procedure of EDOT-N^+.[47]

2.2.2 Electropolymerization of Poly(EDOT-OH) Adhesion Layer

The electrochemical experiments were all performed using an Autolab PGSTAT128N potentiostat (Metrohm, The Netherlands) in a three-electrode setting with platinum as the counter electrode, Ag/AgCl (saturated KCl solution) as the reference electrode, and Au QCM-D chip (QSX 301) as the working electrode. The Au chip was cleaned using Piranha solution with H_2SO_4 : H_2O_2 = 3 : 1, then rinsed with DI water, and dried carefully with nitrogen before electropolymerization.

EDOT-OH solution with 10 mM EDOT-OH monomer, 50 mM sodium dodecyl sulfate (SDS), and 100 mM $LiClO_4$ dissolved in deionized (DI) water was prepared for

doi:10.6342/NTU202301269

electropolymerization. Poly(EDOT-OH) was then pre-deposited on the Au QCM-D chip as an adhesion layer[53] under cyclic potential scans from −0.6 to 1.1 V versus Ag/AgCl reference electrode for 1 cycle to enhance the adhesion of further poly(EDOT-N^+-*co*-EDOT-COOH) layers onto the gold substrate.

2.2.3 Electropolymerization of Poly(EDOT-N^+-*co*-EDOT-COOH) Film

The electropolymerization process is similar to that of poly(EDOT-OH) film. The synthesized EDOT-N^+ and EDOT-COOH monomer solutions were prepared by dissolving EDOT-N^+ and EDOT-COOH monomers with 10 mM in total. One set of monomers was dissolved in DI water with 100 mM $LiClO_4$ as the electrolyte, while the other set of monomers was dissolved in an AOT solution. After the deposition of poly(EDOT-OH) film as an adhesion layer, further layers of poly(EDOT-N^+-*co*-EDOT-COOH) were deposited on the Au QCM-D chip under potential scans from −0.6 to 1.1 V using Ag/AgCl reference electrode in aqueous phase while using Ag/Ag^+ reference electrode in non-aqueous phase.

doi:10.6342/NTU202301269

2.3 Surface Characterization of Poly(EDOT-N^+-*co*-EDOT-COOH) Film

2.3.1 Determination of Carboxylic Acid Groups Surface Density by UV-Vis Spectroscopy

The actual percentage of poly(EDOT-COOH) and poly(EDOT-N^+) in the copolymers was determined by measuring the surface density of carboxylic acid groups (-COOH) on EDOT-COOH by toluidine blue O (TBO) staining. The samples were prepared by coating the analytes onto the QCM-D chips, as mentioned in the previous section, and the QCM-D chips with the same contact area can ensure the films are of the same size. Then, the polymer films coated were immersed in 0.5 mM TBO solution at pH = 10 for 12 hours at room temperature to allow the formation of the ionic complex between the carboxylic acid groups and the dye. After that, the films were rinsed with 0.1 mM NaOH solution to remove the non-complexed TBO molecules. The last step was to immerse the polymer films in 4 mL 50% acetic acid solution for 10 minutes to let the complexed dye desorbed, and the concentration of the dye was determined by measuring the absorbance at 633 nm by UV-Vis spectrophotometer (UV-1900i, Shimadzu, Japan). The amount of the carboxylic acid groups was then calculated by referring to a calibration curve of TBO/50% acetic acid solution recorded in the same conditions based on the

doi:10.6342/NTU202301269

assumption that 1 mole of TBO exactly complex with 1 mole of carboxylic acid groups.[54, 55]

2.4 Fabrication of MOF-Based Solar Desalination Platform

2.4.1 Synthesis of CAU-10-H Powder

1,3-H_2BTC (0.8306 g, 5 mmol) and $Al_2(SO_4)_3 \cdot 18H_2O$ (3.332 g, 5 mmol) were dissolved in the cosolvent of 6 ml dimethylformamide (DMF) and 24 ml deionized water. The solution was stirred and refluxed at 120 ℃ for 48 hours. The resulting CAU-10-H powder was collected by vacuum filtration and was rinsed using DI water. The collected powder was then immersed in methanol to remove DMF for 24 hours, and again used vacuum filtration to collect the powder and dried in the oven at 105 ℃ for 24 hours.

2.4.2 Synthesis of CAU-10-H Membranes

First of all, the synthesized CAU-10-H powder was spread on the cellulose acetate (CA) membrane filter to seed the crystals onto the substrate. Two kinds of spreading methods were used to distribute the dispersed powder solution (0.02 g CAU-10-H powder in 10 ml DI water): drop coating and spin coating method. Drop coating was to drip about 3 ml of powder solution to cover the CA substrate and dried it in the oven at 70 ℃. Spin coating method was to drip 3 ml of powder solution to cover the CA substrate and spin-

doi:10.6342/NTU202301269

coated at 3000 rpm for 30 seconds, and then dried it in the oven at 70 ℃ and repeated this process for 3 times.

To synthesize CAU-10-H membranes with different thicknesses, different amounts of reactants, solvents, and reaction conditions were set as shown in **Table 2-4**. For simple CAU-10-H membrane, 1,3-H_2BTC (0.4153 g, 2.5 mmol) and $Al_2(SO_4)_3 \cdot 18H_2O$ (1.666 g, 2.5 mmol) were dissolved in the cosolvent of 18 ml DMF and 72 ml deionized water as the secondary growth solution. The coated membranes were immersed in the solution and refluxed at 100 ℃ for 6 hours. For CAU-10-H_1.5x, the amounts of reactants added were 1.5 times higher. 1,3-H_2BTC (0.6230 g, 3.75 mmol) and $Al_2(SO_4)_3 \cdot 18H_2O$ (2.499 g, 3.75 mmol) were dissolved in the cosolvent of 18 ml DMF and 72 ml deionized water as the secondary growth solution. The coated membranes were immersed in the solution and refluxed at 100 ℃ for 8 hours. As for CAU-10-H_3rd, the third growth method was used to let the grains on the membrane keep growing into larger sizes. 1,3-H_2BTC (0.4153 g, 2.5 mmol) and $Al_2(SO_4)_3 \cdot 18H_2O$ (1.666 g, 2.5 mmol) were dissolved in the cosolvent of 18 ml DMF and 72 ml deionized water as the secondary growth solution. After the second growth of the CAU-10-H, the membrane was rinsed with DI water and immersed in a new solution with the same prescription to the secondary growth solution to proceed third growth, again refluxing at 100 ℃ for 6 hours.

doi:10.6342/NTU202301269

After all the above process, the membranes were rinsed by DI water and then immersed in methanol for over 24 hours to remove DMF and dried in the oven at 50 ℃.

Table 2-4. The amounts of reactants added and reaction condition setting in synthesizing different CAU-10-H membranes.

	Synthesis method	1,3-H_2BTC (mmol)	$Al_2(SO_4)_3 \cdot 18H_2O$ (mmol)	DMF (ml)	DI water (ml)	Reflux temperature (℃)
CAU-10-H	2nd growth	2.5	2.5	18	72	100
CAU-10-H_1.5x	2nd growth	3.75	3.75	18	72	100
CAU-10-H_3rd	3rd growth	2.5	2.5	18	72	100

2.4.3 Deposition of Solar Absorber Layer

After the CAU-10-H membrane was ready-synthesized and dried, the solar absorber layer was then deposited atop CAU-10-H. First of all, aluminum tape was attached around the membrane to cover up the place where no CAU-10-H was grown, and the tape would also thereafter help the whole desalination system to float on the surface of the water.

doi:10.6342/NTU202301269

Carbon black powder (0.05 g) was dispersed in ethanol (10 g) and spread-coated evenly onto the CAU-10-H membrane by using airbrush. The membrane was then immersed in the stirring solution with dopamine hydrochloride (0.04 g) and 0.1 M NaOH (0.4 ml) dissolving in 70% methanol solution (19.6 ml) to begin the living polymerization of polydopamine for 24 hours. The membrane was then rinsed with DI water and dried in the oven at 50 ℃.

2.5 Water Evaporation Test

2.5.1 Device Setup for the Water Evaporation Test

The CA membrane filter served as the substrate with the CAU-10-H membrane grown on it, and the solar absorber layer deposited on the top was used as the desalination platform (**Figure 2-2a**) to conduct the water evaporation test. The active area in the center of the platform was sealed with a round of epoxy to ensure the water transporting to the surface came from directly below the active area. Then the desalination platform was placed on the surface of a beaker filled with DI water, as shown in **Figure 2-2b**. The desalination device was placed on the electronic balance to record the weight loss which is also the quantity of the water evaporated. A xenon lamp was used as the solar simulator serving as the light source, and the height where the desalination platform placed was set to be one sun irradiation. The IR camera was set up to measure the surface temperature

doi:10.6342/NTU202301269

of the desalination platform. The dry-state temperature was recorded after 10 minutes of illumination under one-sun irradiation, while the wet-state temperature was recorded after 30 minutes of illumination under one-sun irradiation. All the above instruments constructed the whole device setup for the water evaporation test.

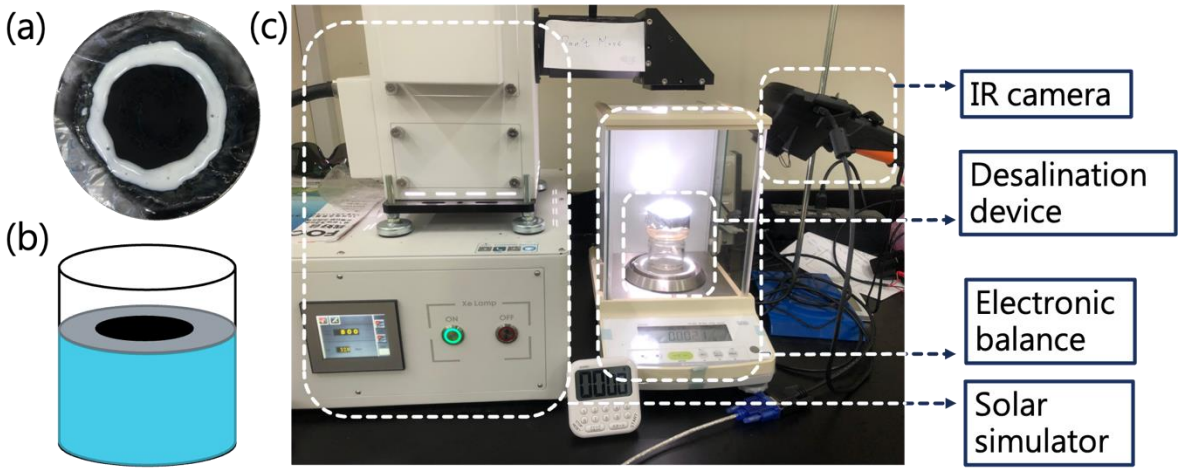

Figure 2-2. (a) The final product of the desalination platform. (b) Schematic illustration of the desalination device. (c) The device setup for the water evaporation test.

2.6 Grafting of Zwitterionic Polymer Brush

2.6.1 Immobilization of Initiator on Cellulose Acetate Surface

To begin with, to start the surface-initiated atom transfer radical polymerization (SI-ATRP) reaction, initiator should first be immobilized on the surface of the substrate. The

doi:10.6342/NTU202301269

initiator BiBB would react with the hydroxyl groups on the CA surface. TEA (44 mmol) and DMAP (10 mmol) were dissolved in 50 ml THF, and the CA substrate was immersed in the solution and stirred in ice bath for 20 minutes. Then, the BiBB solution with BiBB (40 mmol) dissolving in 10 ml THF was added dropwise into the reaction. The solution was kept stirring in ice bath for 2 hours, and then the reaction proceeded at 20 ℃ for 22 hours. After the reaction completed, the collected initiator-functionalized membrane, referring to CA-Br, was ultrasonicated in dichloromethane and ethanol each for 10 minutes and dried.[44, 56]

2.6.2 Grafting Zwitterionic Polymer Brush on Cellulose Acetate Membrane via SI-ATRP Method

The functionalized CM-Br sheet was first placed in a dry flask with CuBr (0.5 mmol) and then vacuumed and backfilled with nitrogen for 5 times. Then, a 20 ml degassed solution with SBMA monomer (4 mmol) and Bpy (1 mmol) dissolving in the mixing solution of 10 ml methanol and 10ml DI water was added into the flask under nitrogen protection to start the reaction. The polymerization process was carried out at room temperature for 1 hour. After the reaction completed, the collected SBMA-functionalized membrane, referring to CA-SBMA, was ultrasonicated in DI water-PBS buffer-DI water each for 10 minutes and dried.[44, 56]

doi:10.6342/NTU202301269

2.7 Characterization

2.7.1 Contact Angle Measurement

The static contact angle measurement was performed by a goniometer (Sindatek, Taiwan). As mentioned in the previous section, samples were prepared by coating the analytes onto the QCM-D chips. A droplet (~1.0 μL) was deposited on the polymer coating film on the QCM-D chip and was illuminated from behind to make the image recorded by the camera. The image is then analyzed using software, and the magnitude of the contact angle is determined. All measurements were taken at least three times to collect average values and standard deviations.

2.7.2 Atomic Force Microscopy (AFM)

Atomic force microscopy (AFM, Bioscope Resolve system, Bruker, USA) was performed to characterize the surface morphology and the adhesion force. The characterization process was operated in PFQNM mode in fluid with PFQNM-LC-A-CAL tips.

2.7.3 Fourier-Transform Infrared Spectroscopy (FTIR)

Fourier-transform Infrared Spectroscopy (FTIR, FT/IR-6700, JASCO, Japan) was performed to obtain information of the functional groups on the surface based on the principle that molecules absorb specific frequencies of infrared light, resulting in characteristic vibrational and rotational energy changes. Attenuated total reflection (ATR)

doi:10.6342/NTU202301269

is a commonly used sampling technique in FTIR spectroscopy. It allows for direct analysis of solid or liquid samples without extensive sample preparation.

2.7.4 UV-Vis Spectroscopy (UV-Vis)

UV-Vis spectroscopy measures the absorption or transmission of specific wavelengths of UV or visible light by a sample compared to a reference or blank sample. The amount of light absorbed or transmitted is influenced by the composition of the sample, which can provide information about its constituents and their concentrations. UV-Vis spectrophotometer (UV-1900i, Shimadzu, Japan) was used to analyze the absorption spectra of the TBO molecules at 633 nm.

2.7.5 X-ray Photoelectron Spectroscopy (XPS)

X-ray Photoelectron Spectroscope (PHI 5000 Versa Probe, ULVAC-PHi, Japan) is used to perform analytical technique which is based on the photoelectric effect to study the elemental composition of the sample surface.

2.7.6 Quartz Crystal Microbalance with Dissipation Monitoring (QCM-D)

Quartz crystal microbalance with dissipation monitoring (QCM-D) uses its inverse piezoelectric properties to apply alternating current to generate a stable resonance. By monitoring the resonance frequency and dissipation change in real time, the small mass

doi:10.6342/NTU202301269

change can be measured, thus corresponding to the protein adsorption/desorption behavior taking place on the chip surface.[57, 58]

2.7.7 X-ray Diffraction (XRD)

X-ray Diffractometer (MiniFlex, Rigaku) is utilized as a non-destructive characterization technique for analyzing and determining the crystal structure of materials. The characterization process was operated scanning from 5° to 30° 2θ with a step size of 0.5° 2θ using an incident beam of 1°.

2.7.8 Scanning Electron Microscopy (SEM)

Scanning electron microscope (Hitachi S-4800, Japan) was performed to obtain surface morphology and microstructure of our fabricated membranes. The images were acquired with an accelerating voltage of 10 kV. Since the samples were non-conductive, a layer of platinum was sputtered at an accelerating voltage of 25 V for 40 seconds.

doi:10.6342/NTU202301269

Chapter 3 Results and Discussion

3.1 Tuning the Surface Charge through Electrochemical Copolymerization of Functionalized PEDOTs toward Antifouling Surfaces

3.1.1 Determine between Organic Solvent and DI water

The synthesized EDOT-N^+ monomer was dissolved in DI water and AOT solution respectively and electropolymerized into polymer film. The FT-IR spectrum of the film electropolymerized using aqueous monomer solution was shown in **Figure 3-1a**, showing that there is a peak near 1096 cm^{-1}, where it indicates C-N stretching according to IR spectrum table. The C-N stretching peak is deemed to be correspond to the chemical structure of poly(EDOT-N^+). As for the film electropolymerized using AOT monomer solution, there is no peak showing the information of C-N stretching as in **Figure 3-1b**. Therefore, we assume that maybe the poly(EDOT-N^+) did not successfully deposit on our chip. As a result, all of the films prepared in the following steps are deposited using the monomer solution prepared with monomers dissolved in DI water with 100 mM $LiClO_4$ as electrolyte.

doi:10.6342/NTU202301269

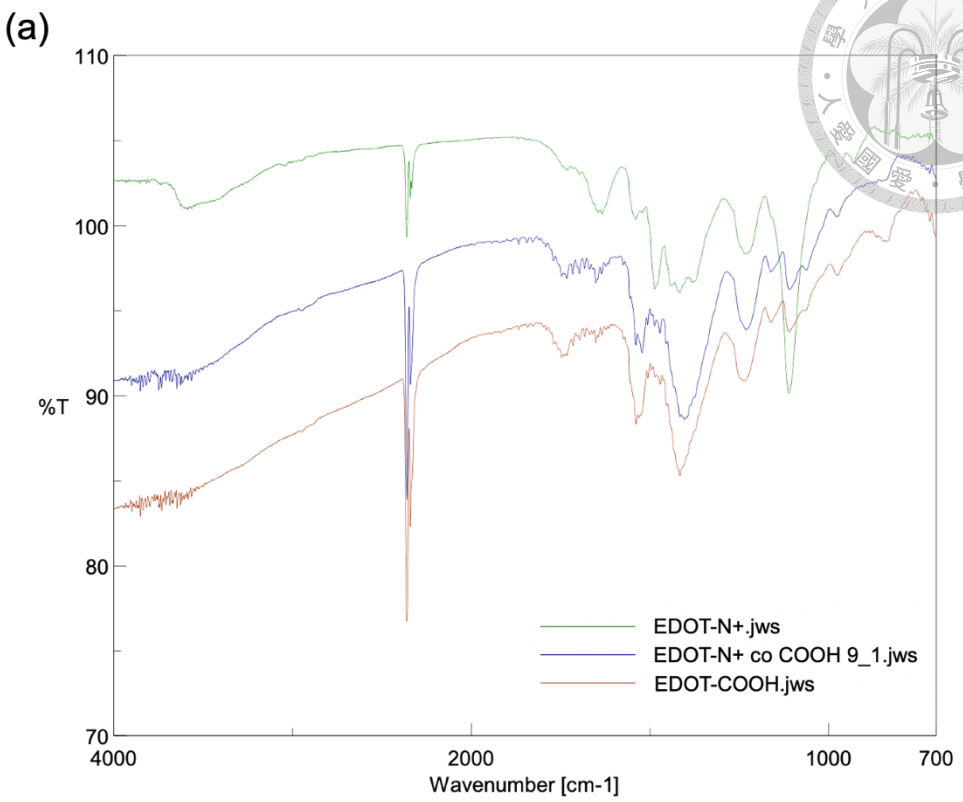

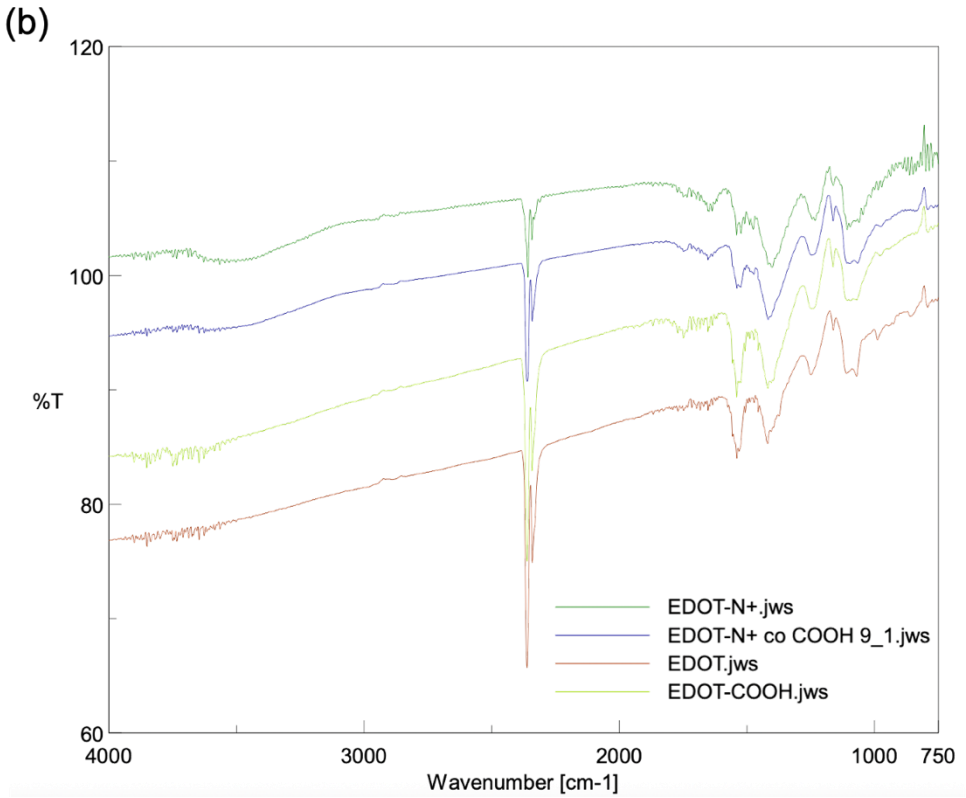

doi:10.6342/NTU202301269

Figure 3-1. FT-IR spectrum of (a) poly(EDOT-N^+), poly(EDOT-COOH), and poly(EDOT-N^+-*co*-EDOT-COOH) with a feed composition of [EDOT-N^+] : [EDOT-COOH] = 9 : 1 electropolymerized in aqueous phase and (b) poly(EDOT-N^+), poly(EDOT-COOH), poly(EDOT), and poly(EDOT-N^+-*co*-EDOT-COOH) with a feed composition of [EDOT-N^+] : [EDOT-COOH] = 9 : 1 electropolymerized in non-aqueous phase.

3.1.2 The Fabrication of Poly(EDOT-N^+-*co*-EDOT-COOH) Film

The electropolymerization of poly(EDOT-N^+), poly(EDOT-COOH), and four poly(EDOT-N^+-*co*-EDOT-COOH) prepared with different feed compositions were performed on QCM-D chips with a layer of as-prepared poly(EDOT-OH) film to enhance the adhesion with the Au surface. From the electropolymerization curve shown in **Figure 3-2a** to **Figure 3-2f**, we noticed that with an increasing EDOT-COOH feed ratio, the increscent current while polymer deposition indicates that the growth rate of poly(EDOT-COOH) was much faster than poly(EDOT-N^+) when the same potential is applied for polymerization. As a result, the actual composition of the copolymers does not correspond to the feed ratio of monomer solutions for electropolymerization. Since poly(EDOT-COOH) is deposited much faster, the feed ratio of EDOT-N^+ should be higher to reach an accurate 1:1 ratio of the poly(EDOT-N^+) and poly(EDOT-COOH) of the copolymer.

doi:10.6342/NTU202301269

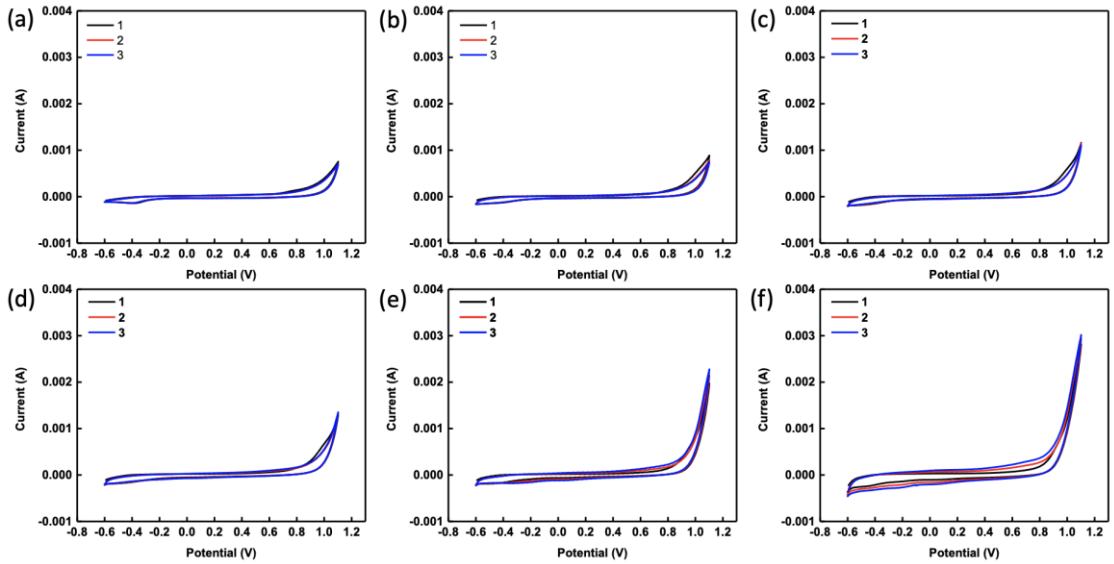

Figure 3-2. Electropolymerization of (a) poly(EDOT-N$^+$), poly(EDOT-N$^+$-*co*-EDOT-COOH) with a feed composition of [EDOT-N$^+$] : [EDOT-COOH] = (b) 9 : 1, (c) 8 : 2, (d) 7 : 3, (e) 1 : 1, and (f) poly(EDOT-COOH), by applying a cyclic potential between -0.6 to 1.1 V vs. Ag/AgCl.[47]

3.1.3 Surface Characterization of Poly(EDOT-N$^+$-*co*-EDOT-COOH).

AFM images were acquired to further confirm the cross-section information of the films. Here, we used one of the feed compositions to demonstrate the correlation between film thickness and the number of cycles of potential applied. As shown in **Figure 3-3**, we revealed the film thickness by measuring the depth profile over the boundary of the polymer film and the gold substrate. From **Figure 3-3d** to **Figure 3-3f**, we can learn that the thickness of the copolymer under 1 cycle of cyclic potential is about 20 nm, while that

doi:10.6342/NTU202301269

of 3 cycles increased to 40 nm, and 60 nm when the cyclic potential added to 5 cycles. The results also correspond to previous study[59] that the increase of cycles of potential applied would increase the film thickness. This result support our experiment settlement that by adjusting the cycles and scanning rate of the potential applied, we can tailor the thickness of the electropolymerized film.

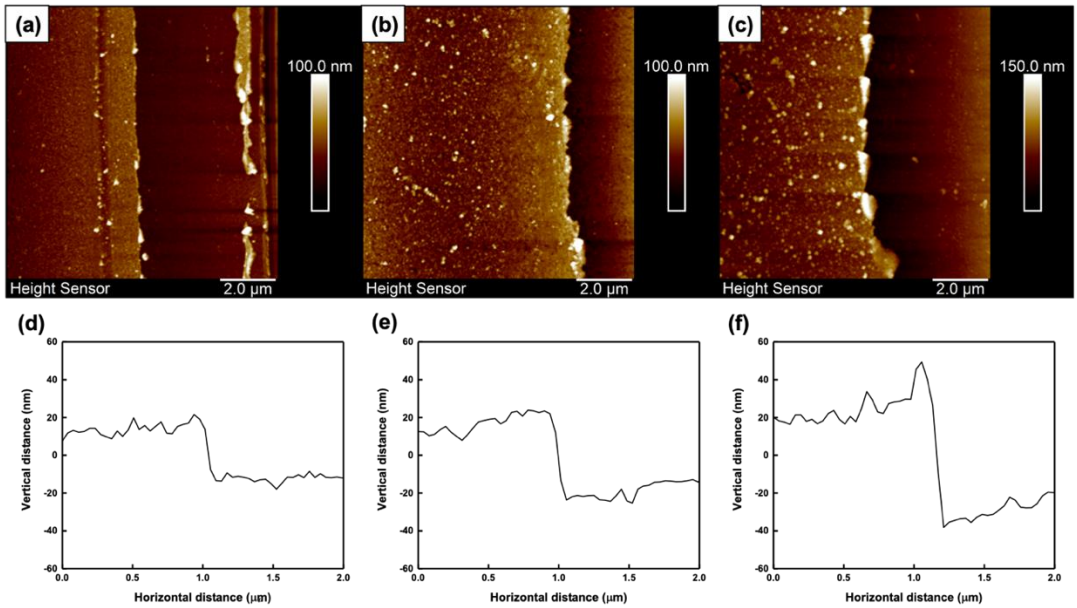

Figure 3-3. AFM image of poly(EDOT-N$^+$-*co*-EDOT-COOH) with a feed composition of [EDOT-N$^+$] : [EDOT-COOH] = 8 : 2 under (a) 1, (b) 3, (c) 5 cycles of cyclic potential between -0.6 to 1.1 V vs. Ag/AgCl. The depth profile across the scrape on the film under (d) 1, (e) 3, (f) 5 cycles of cyclic potential.[47]

The top view of the film was also acquired to confirm further the surface morphology

doi:10.6342/NTU202301269

of poly(EDOT-N^+), poly(EDOT-COOH), and four poly(EDOT-N^+-*co*-EDOT-COOH) prepared with different feed compositions, as shown in **Figure 3-4**. It was found that the surface of poly(EDOT-N^+) was relatively smooth, contrary to the nanostructured poly(EDOT-COOH), and the roughness of the samples nearly increased as the EDOT-COOH ratio increased. The poly(EDOT-COOH) film presented the highest roughness. The results of AFM measurement are consistent with the observations from electropolymerization curves. When the deposition rate was higher, the polymer film grew faster and became rougher during electropolymerization.

doi:10.6342/NTU202301269

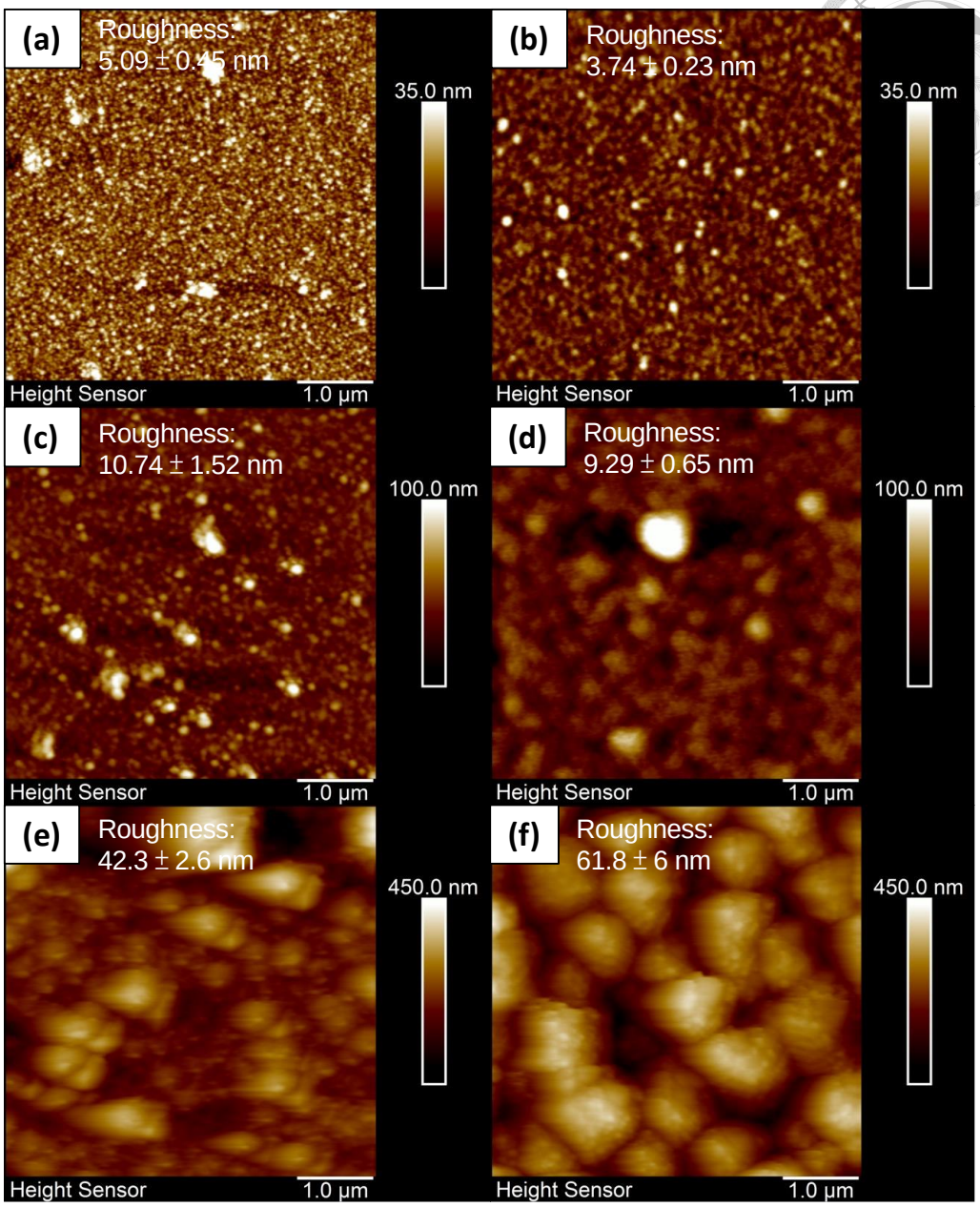

Figure 3-4. AFM images and the R_{rms} roughness of (a) poly(EDOT-N^+), poly(EDOT-N^+-*co*-EDOT-COOH) with a feed composition of [EDOT-N^+] : [EDOT-COOH] = (b) 9 : 1, (c) 8 : 2, (d) 7 : 3, (e) 1 : 1, and (f) poly(EDOT-COOH) deposited under 3 cycles of potential scans.[47]

doi:10.6342/NTU202301269

3.1.4 Elemental Information Acquired by XPS Technique

The poly(EDOT-N^+-*co*-EDOT-COOH) films prepared with different feed compositions were electropolymerized on the QCM-D ships. To know the actual composition of the deposited films, the XPS technique was utilized. Since EDOT-N^+ had an N element, N_{1s} narrow-scan spectrum was acquired, as shown in **Figure 3-5**. However, the background noise was too large to clearly identify the peaks, not to mention to integrate the quantity of N. C_{1s} narrow-scan spectra was also acquired, as shown in **Figure 3-6**. Peak fitting of the C_{1s} spectra was performed, and the results were shown in **Figure 3-7**. Unfortunately, the binding energy of the C-N bond and C-O-C bond was too close to identify the two peaks, as a result, the C_{1s} spectrum could not be an efficient way to quantify the proportion of EDOT-N^+.

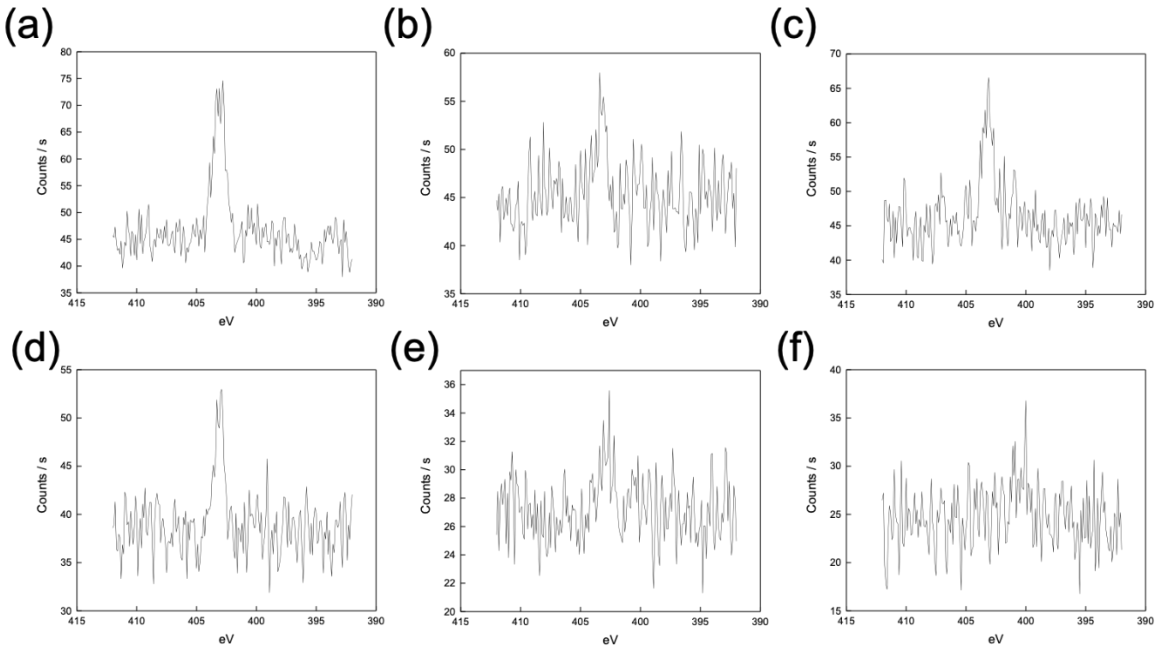

doi:10.6342/NTU202301269

Figure 3-5. XPS N_{1s} narrow-scan spectra of (a) poly(EDOT-N^+), poly(EDOT-N^+-*co*-EDOT-COOH) with a feed composition of [EDOT-N^+] : [EDOT-COOH] = (b) 9 : 1, (c) 8 : 2, (d) 7 : 3, (e) 1 : 1, and (f) poly(EDOT-COOH).

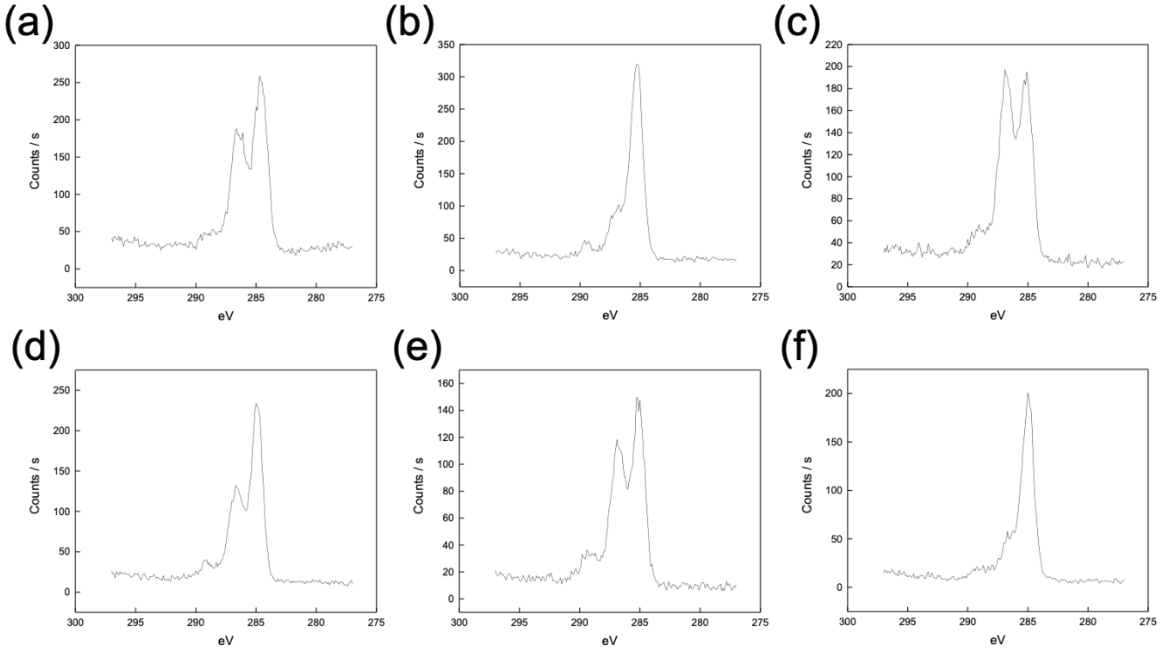

Figure 3-6. XPS C_{1s} narrow-scan spectra of (a) poly(EDOT-N^+), poly(EDOT-N^+-*co*-EDOT-COOH) with a feed composition of [EDOT-N^+] : [EDOT-COOH] = (b) 9 : 1, (c) 8 : 2, (d) 7 : 3, (e) 1 : 1, and (f) poly(EDOT-COOH).

doi:10.6342/NTU202301269

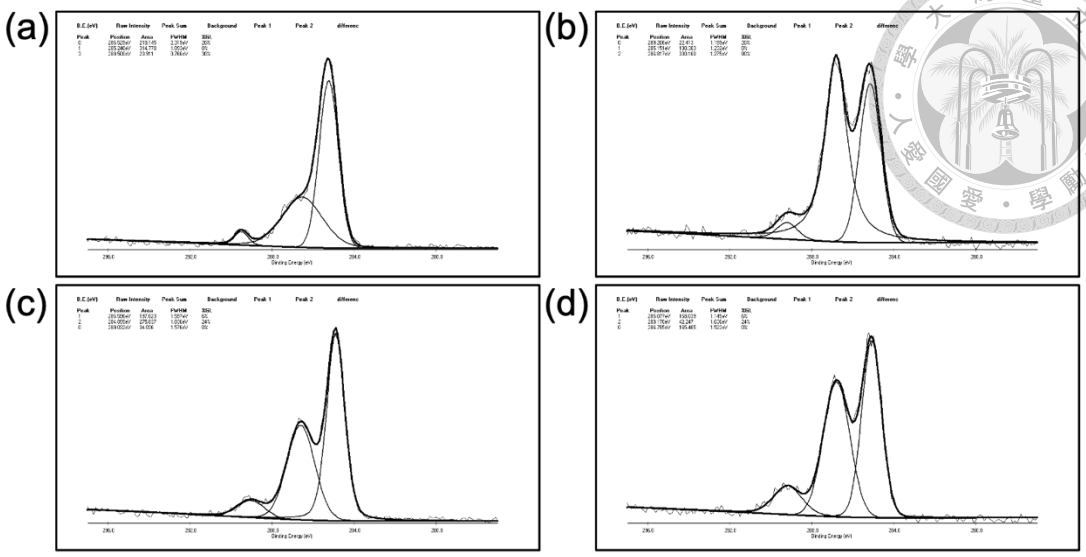

Figure 3-7. Peak fitting of XPS C_{1s} narrow-scan spectra of poly(EDOT-N^+-*co*-EDOT-COOH) with a feed composition of [EDOT-N^+] : [EDOT-COOH] = (a) 9 : 1, (b) 8 : 2, (c) 7 : 3, (d) 1 : 1.

3.1.5 Determination of Carboxylic Acid Group on EDOT-COOH

The surface density of carboxylic acid groups on EDOT-COOH was determined by TBO staining, which covalently formed peptide bonds between carboxylic acid and amine (NH_2) group on TBO molecules and was desorbed in an acidic environment. The UV-Vis spectroscopy of poly(EDOT-N^+), poly(EDOT-COOH), and four poly(EDOT-N^+-*co*-EDOT-COOH) prepared with different feed compositions were shown in **Figure 3-8a**. Noteworthily, the TBO staining method was only suitable for a smooth surface since the roughness of the film would increase the surface area and lead to the distortion of the resulting absorbance signal. However, as shown in **Figure 3-4**, the surface of poly(EDOT-

doi:10.6342/NTU202301269

N^+) was relatively smooth, while the nanostructured poly(EDOT-COOH) had higher roughness. To eliminate the effect of surface roughness, the films were electropolymerized under different conditions to control the samples to be in similar status.

The absorption peak of TBO molecules at 633 nm showed a trend, with poly(EDOT-COOH) having the largest absorbance and decreasing as the [EDOT-COOH] feed ratio decreased. There was still an absorbance peak for poly(EDOT-N^+) film due to the nonspecific binding of TBO molecules onto the film, though without the presence of the carboxylic acid groups. The effect of nonspecific binding was then eliminated by subtracting the background signal. The actual composition compared to the feed composition, as shown in **Figure 3-8b,** confirmed our previous conjecture that with the different growth rates of the electropolymerization of poly(EDOT-N^+) and poly(EDOT-COOH), the actual composition of the copolymers would not correspond to the feed ratio of the monomer solutions. Here, as shown in **Figure 3-8b**, to reach an accurate 1:1 ratio of the poly(EDOT-N^+) and poly(EDOT-COOH) of the copolymer, the feed ratio is located at about 8:2 feed ratio of poly(EDOT-N^+) and poly(EDOT-COOH).

doi:10.6342/NTU202301269

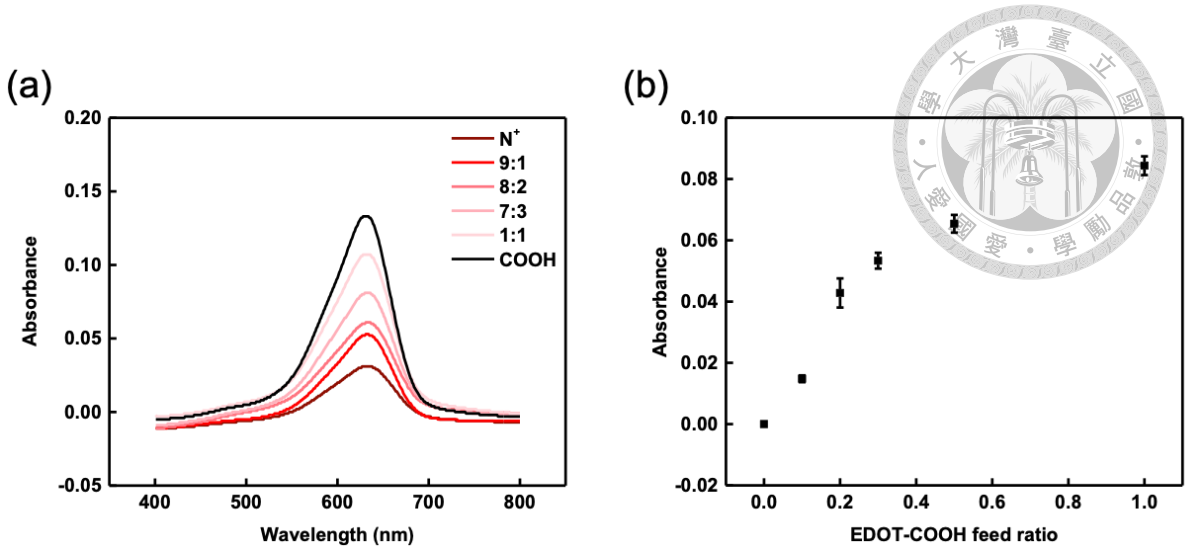

Figure 3-8. (a) Original TBO staining data of poly(EDOT-N$^+$), poly(EDOT-COOH), and four poly(EDOT-N$^+$-*co*-EDOT-COOH) prepared with different feed compositions. (b) The absorbance at 633 nm after the subtraction of the background signal.[47]

3.1.6 Contact Angle Measurement

The contact angle measurements were conducted in pairs of complementary cases, water-in-air, and air-in-water, as shown in **Figure 3-9a and b**. In general, the polymer films with low water-in-air contact angles present high air-in-water contact angles, indicating more hydrophilic surfaces. At first, we conducted the contact angle measurement with the films all deposited under the same condition (**Figure 3-9c**) and poly(EDOT-COOH) presented a lower water-in-air contact angle (~ 24.7°), which indicates high hydrophilicity, compared to poly(EDOT-N$^+$), which presented a water-in-

doi:10.6342/NTU202301269

air contact angle at 40.8°. A similar trend was observed by measuring the air-in-water contact angle. An air bubble presented a 156° contact angle on poly(EDOT-COOH) in water, which is higher than that on poly(EDOT-N^+). Interestingly, by mixing EDOT-COOH and EDOT-N^+ with different feed ratios, the poly(EDOT-N^+-*co*-EDOT-COOH) copolymers showed a different extent of change in both the air-in-water and water-in-air contact angles. The contact angles are not linear proportional to the composition of poly(EDOT-N^+-*co*-EDOT-COOH). For [EDOT-N^+] : [EDOT-COOH] = 1 : 1, poly(EDOT-N^+-*co*-EDOT-COOH) had the lowest water-in-air contact angle of about 9.0°, while [EDOT-N^+] : [EDOT-COOH] = 9 : 1, poly(EDOT-N^+-*co*-EDOT-COOH) having the highest water-in-air contact angle of about 48.4° among all of the mixing ratios. The results indicate that the poly(EDOT-N^+-*co*-EDOT-COOH) was most hydrophobic at [EDOT-N^+] : [EDOT-COOH] = 9 : 1, and most hydrophilic at [EDOT-N^+] : [EDOT-COOH] = 1 : 1. The unexpected contact angle measurement results might be due to the complicated interaction between the distribution of surface functional groups and the morphology. Further studies are required to understand irregular observation.

To understand the irregular trend of the contact angle observation, we looked further into the factors that influenced the measurement of the contact angle. There are some factors affecting the wettability of a surface,[60] especially surface roughness and the intrinsic hydrophilicity/hydrophobicity of the material in our case.

doi:10.6342/NTU202301269

To eliminate the effect of surface roughness, the films were also prepared under different conditions to control the films as mentioned in the TBO staining section. The results were as shown in **Figure 3-9d**. Among all of the mixing ratios, poly(EDOT-COOH) presented a lower water-in-air contact angle (~35.6°), which indicates high hydrophilicity, compared to poly(EDOT-N^+), which presented the highest water-in-air contact angle of 52.9°. Interestingly, by mixing EDOT-COOH and EDOT-N^+ with different feed ratios, the poly(EDOT-N^+-*co*-EDOT-COOH) copolymers showed a different extent of change in the water-in-air contact angles. The contact angles are not linear proportional to the composition of poly(EDOT-N^+-*co*-EDOT-COOH). Starting from pure poly(EDOT-N^+) and gradually increasing the content of EDOT-COOH, the contact angle of [EDOT-N^+] : [EDOT-COOH] = 9 : 1 declined to about 43.8°, and continued decreasing to the lowest water-in-air contact angle of about 29.5° at [EDOT-N^+] : [EDOT-COOH] = 8 : 2. While the content of EDOT-COOH kept increasing, the contact angle rose to about 35.7° at [EDOT-N^+] : [EDOT-COOH] = 7 : 3, and became even more hydrophobic at [EDOT-N^+] : [EDOT-COOH] = 1 : 1 with a high water-in-air contact angle of about 40.1°, even higher than that of pure poly(EDOT-COOH). The results indicate that the poly(EDOT-N^+-*co*-EDOT-COOH) was most hydrophilic at [EDOT-N^+] : [EDOT-COOH] = 8 : 2, most hydrophobic at pure poly(EDOT-N^+), and there is also a local maximum water-in-air contact angle at [EDOT-N^+] : [EDOT-COOH] = 1 : 1.

doi:10.6342/NTU202301269

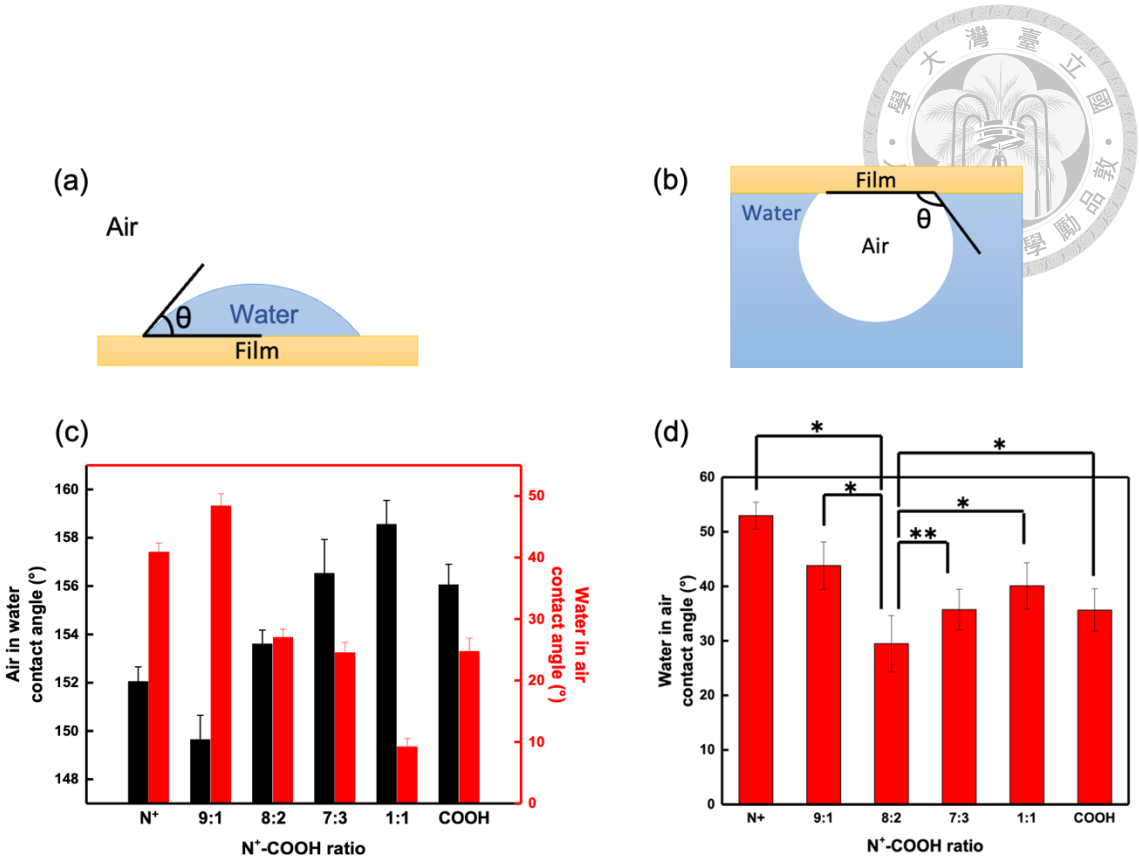

Figure 3-9. Schematic illustration showing the (a) water in atmospheric air and (b) an air bubble in water contact angle measurement. (c) The contact angle measurement of poly(EDOT-N^+), poly(EDOT-COOH), and four poly(EDOT-N^+-*co*-EDOT-COOH) prepared with different feed compositions deposited all under 3 cycles of potential scans. (d) The water-in-air contact angle measurement of poly(EDOT-N^+), poly(EDOT-COOH), and four poly(EDOT-N^+-*co*-EDOT-COOH) prepared with different feed compositions in similar surface roughness under different electrochemical conditions. *p<0.01 and **p<0.05.[47]

doi:10.6342/NTU202301269

3.1.7 Protein Binding Behavior on Poly(EDOT-N$^+$-*co*-EDOT-COOH)

The QCM-D instrument introduced the inverse piezoelectric effect to apply an external AC electric field to make the quartz crystal oscillate at a specific frequency. When the polymer film coated on the quartz crystal adsorbs some molecules, the resonance frequency of the quartz crystal would decrease. Since the third overtone frequency was used in this study and the overtone frequency is related to the observed distance from the surface of the chip, the thickness of the coated polymer films was controlled to be in similar status. The frequency change, which corresponded to the mass variation due to surface protein adsorption, was measured in situ by QCM-D and was converted to adsorbed mass change according to Sauerbrey equation.[61, 62]

$$\Delta m = -C \cdot \frac{\Delta F}{n}$$

ΔF is the resonance frequency change, Δm is the adsorbed mass change occurred on the surface, while n is the number of the odd harmonic, in here we use the third overtone (n =3). C is called the sensitivity constant. For a 5 MHz crystal, C equals 17.7 ng/(cm^2· Hz).

The amount of BSA and LYZ binding was tested on our poly(EDOT-N$^+$-*co*-EDOT-COOH) films compared to poly(EDOT-N$^+$) and poly(EDOT-COOH). The original data were expressed in frequency change over time, as shown in **Figure 3-10**. The results were further transformed to mass change over time according to the Sauerbrey equation. For

doi:10.6342/NTU202301269

negatively charged BSA, poly(EDOT-COOH) presented a higher mass change (~ 564 ng/cm^2), which indicates high protein adsorption, compared to poly(EDOT-N$^+$), which showed a lower mass change of about 135 ng/cm^2, as depicted in **Figure 3-11a**. Since poly(EDOT-COOH) and BSA were both negatively charged, they should have had repulsive force due to the electrostatic interaction. However, there was a significant mass change corresponding to a large amount of protein binding. This phenomenon can be interpreted by previous studies,[63, 64] which have demonstrated the specific recognition of carboxyl groups with BSA at pH = 7.4. By mixing EDOT-COOH and EDOT-N$^+$ with different feed ratios, the poly(EDOT-N$^+$-*co*-EDOT-COOH) copolymers showed different extents of mass changes. The maximum mass change occurred on the poly(EDOT-N$^+$-*co*-EDOT-COOH) of [EDOT-N$^+$] : [EDOT-COOH] = 1 : 1 with Δm~ 869 ng/cm^2, while the minimum adsorption happened on the film of [EDOT-N$^+$] : [EDOT-COOH] = 8 : 2 with Δm ~ 48 ng/cm^2. The maximum adsorption of BSA on poly(EDOT-N$^+$-*co*-EDOT-COOH) of [EDOT-N$^+$] : [EDOT-COOH] = 1 : 1 might be due to the synergistic effect of electrostatic attraction between negatively charged BSA and positively charged EDOT-N$^+$, and the specific recognition between BSA and EDOT-COOH. As shown in **Figure 3-11b**, to positively charged LYZ, poly(EDOT-COOH) presented the most significant mass change (~ 301 ng/cm^2), which indicates high protein adsorption due to the electrostatic attraction, compared to poly(EDOT-N$^+$), which presented the lowest mass

doi:10.6342/NTU202301269

change at about 20 ng/cm^2. The attractive electrostatic force for positively charged poly(EDOT-N$^+$) and repulsive force for negatively charged poly(EDOT-COOH) were effective here. Interestingly, the amount of mass change did not simply increase as [EDOT-COOH] increased. There is a local minimum at [EDOT-N$^+$] : [EDOT-COOH] = 8 : 2 with $\Delta m \sim 26$ ng/cm^2, and then the mass change finally increased with [EDOT-COOH]. The poly(EDOT-N$^+$-*co*-EDOT-COOH) of [EDOT-N$^+$] : [EDOT-COOH] = 8 : 2 can effectively reduce the non-specific adsorption from both BSA and LZY, indicating good antifouling properties, which also corresponded to previous study[22] which claimed that hydrophilic materials would form a layer of hydration layer to provide better antifouling property with poly(EDOT-N$^+$-*co*-EDOT-COOH) of [EDOT-N$^+$] : [EDOT-COOH] = 8 : 2 having the lowest water-in-air contact angle as shown in **Figure 3-9d** among all of the mixing ratios. Based on the TBO staining data, the composition of EDOT-N$^+$ and EDOT-COOH are closed to equal in this copolymer. Therefore, we propose that the antifouling property of this poly(EDOT-N$^+$-*co*-EDOT-COOH) is attributed to a zwitterion-like behavior.

doi:10.6342/NTU202301269

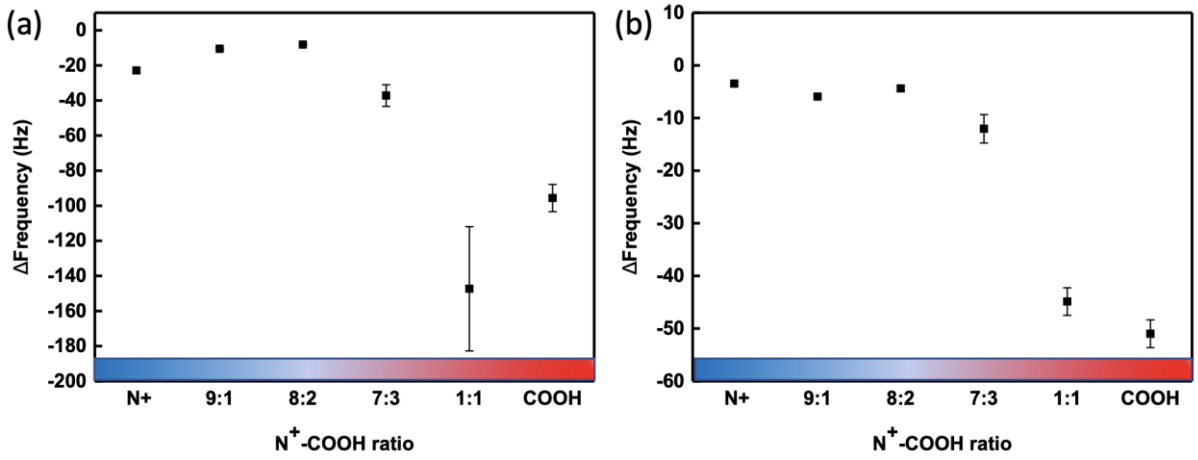

Figure 3-10. Frequency change when (a) BSA and (b) LYZ were bound to poly(EDOT-N^+), poly(EDOT-COOH), and four poly(EDOT-N^+-*co*-EDOT-COOH) in the PBS buffer.

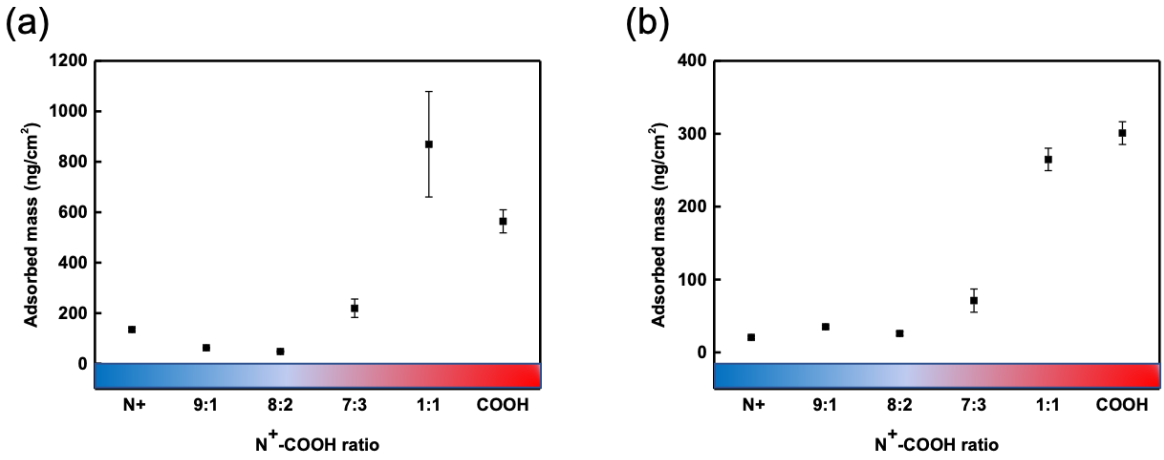

Figure 3-11. Mass change when (a) BSA and (b) LYZ were bound to poly(EDOT-N^+), poly(EDOT-COOH), and four poly(EDOT-N^+-*co*-EDOT-COOH) in the PBS buffer.[47]

doi:10.6342/NTU202301269

As for the other parameter QCM-D instrument recorded, the dissipation change over time was shown in **Figure 3-12**. The dissipation parameter, also known as ΔD, is derived from the energy dissipation occurring during the oscillation of the quartz crystal sensor, providing information about the viscoelastic properties and interfacial processes occurring at the surface of the sensor.

When BSA and LYZ bound to the poly(EDOT-N^+) surfaces, the dissipations both slight increased. Interestingly, when BSA and LYZ bound to the poly(EDOT-COOH) surface, the dissipation decreased, and the dissipation of poly(EDOT-N^+-*co*-EDOT-COOH) in different mixing ratio all decrease with the amount of poly(EDOT-COOH) increased. In general, when protein bound to the QCM-D chip surface, dissipation would usually increase. Previous studies suggested the decrease of the dissipation parameter may be due to loss of water and formation of rigid structures.[57] Therefore, we suggested that when BSA or LYZ bound to the poly(EDOT-COOH) surface, there may be some interactions between the proteins and the functional groups on the polymer film surface, leading to the release of water molecules. Further studies need to be carried out to confirm the conjecture.

doi:10.6342/NTU202301269

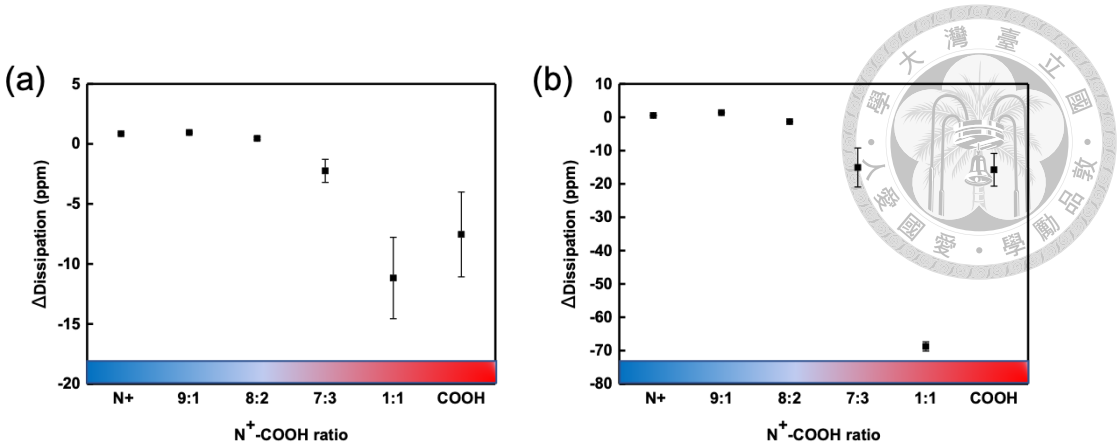

Figure 3-12. Dissipation change when (a) BSA and (b) LYZ were bound to poly(EDOT-N^+), poly(EDOT-COOH), and four poly(EDOT-N^+-*co*-EDOT-COOH) in the PBS buffer.

doi:10.6342/NTU202301269

3.2 Improved Antifouling property of Metal-Organic Framework-Based Solar Desalination System by Zwitterionic Polymer Grafting

3.2.1 Surface Characterization of the Synthesized Films

Cellulose acetate (CA) membrane filter was chosen as the substrate of the solar vapor generation system, and a metal-organic framework and zwitterionic polymer brush would be further deposited onto this substrate. To understand more about the CA substrate, SEM spectroscopy was conducted to observe the morphology and microstructure of this ready-made membrane filter. In **Figure 3-13a**, the CA substrate was found to have something covering on the other one. From **Figure 3-13c and d**, the cross-section SEM image clearly showed that the membrane filter was separated into two parts: the inner layer was composed of coarse fiber, and the surface was covered with a fluff-like layer. To be more detailed, the surface layer was composed of regular porous structure with similar pore size according to **Figure 3-13b**.

doi:10.6342/NTU202301269

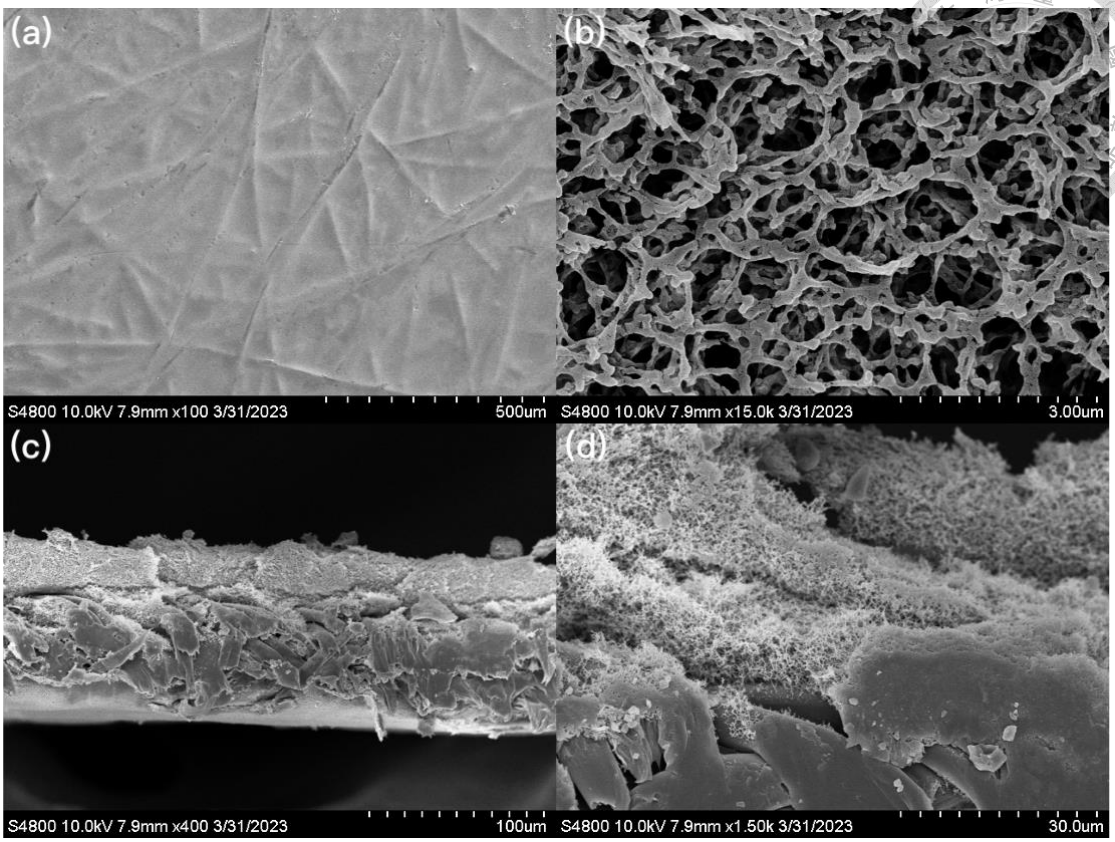

Figure 3-13. SEM images of the cellulose acetate membrane filter.

To synthesize CAU-10-H membrane onto cellulose acetate membrane filter, some tryouts are conducted to determine the synthetic conditions. For the seeding process of the CAU-10-H powder, two kinds of methods were used: drop coating and spin coating methods. SEM microscopy was conducted to determine the structure of the synthesized CAU-10-H membranes. From **Figure 3-14a and d**, both of the seeding methods were confirmed to uniformly grow CAU-10-H crystals. Zooming in to further observe the surface morphology in smaller areas (**Figure 3-14b and e)**, the grains grown on the substrates seeded in two different methods were both in flaky structure. This kind of flaky

doi:10.6342/NTU202301269

structure of the CAU-10-H indicates that the grain was not well-grown and that the grain was incomplete. According to the cross-section SEM result (**Figure 3-14c and f**), the thickness of the CAU-10-H membrane seeded by drop coating and spin coating methods were 992 nm and 843 nm, respectively, again confirming that the grain was not well-grown.

As for the XRD results, it was conducted to confirm whether the CAU-10-H grains grew in the right crystal structure. The crystal structure of CAU-10-H is as shown in **Figure 3-15a**. From the XRD results shown in **Figure 3-15b**, the synthesized CAU-10-H membranes seeded using drop coating and spin coating methods both showed characteristic peak same as the simulated CAU-10-H. Other than the peak of CAU-10-H, the signal of the CA substrate also occurred in both of the membranes, and was especially strong in that of the membrane seeded using drop coating method. As a result, spin coating method was used to do the powder seeding in the following experiments.

doi:10.6342/NTU202301269

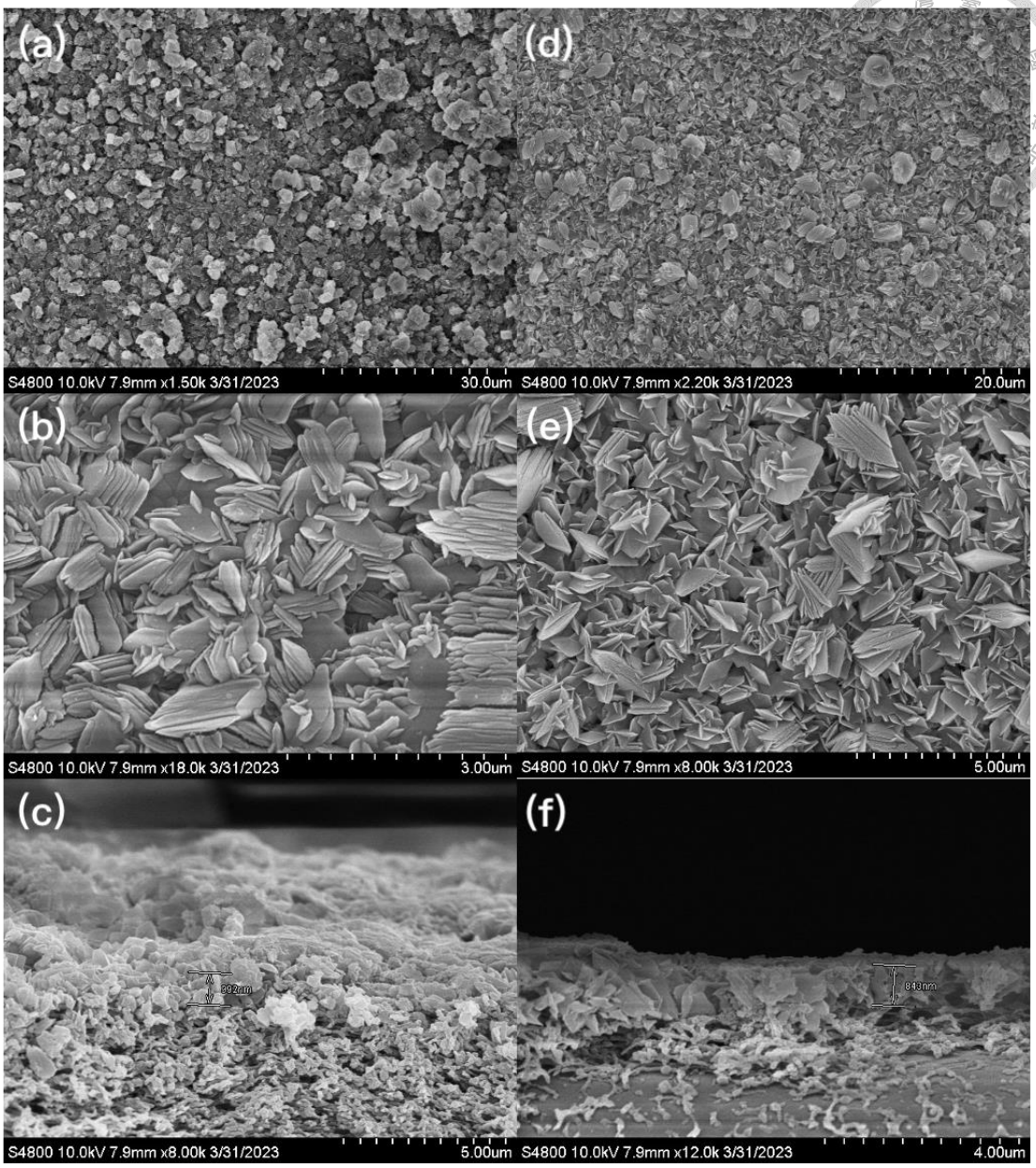

Figure 3-14. SEM image of the synthesized CAU-10-H membranes with the seeding process conducted using (a-c) drop coating and (d-e) spin coating respectively.

doi:10.6342/NTU202301269

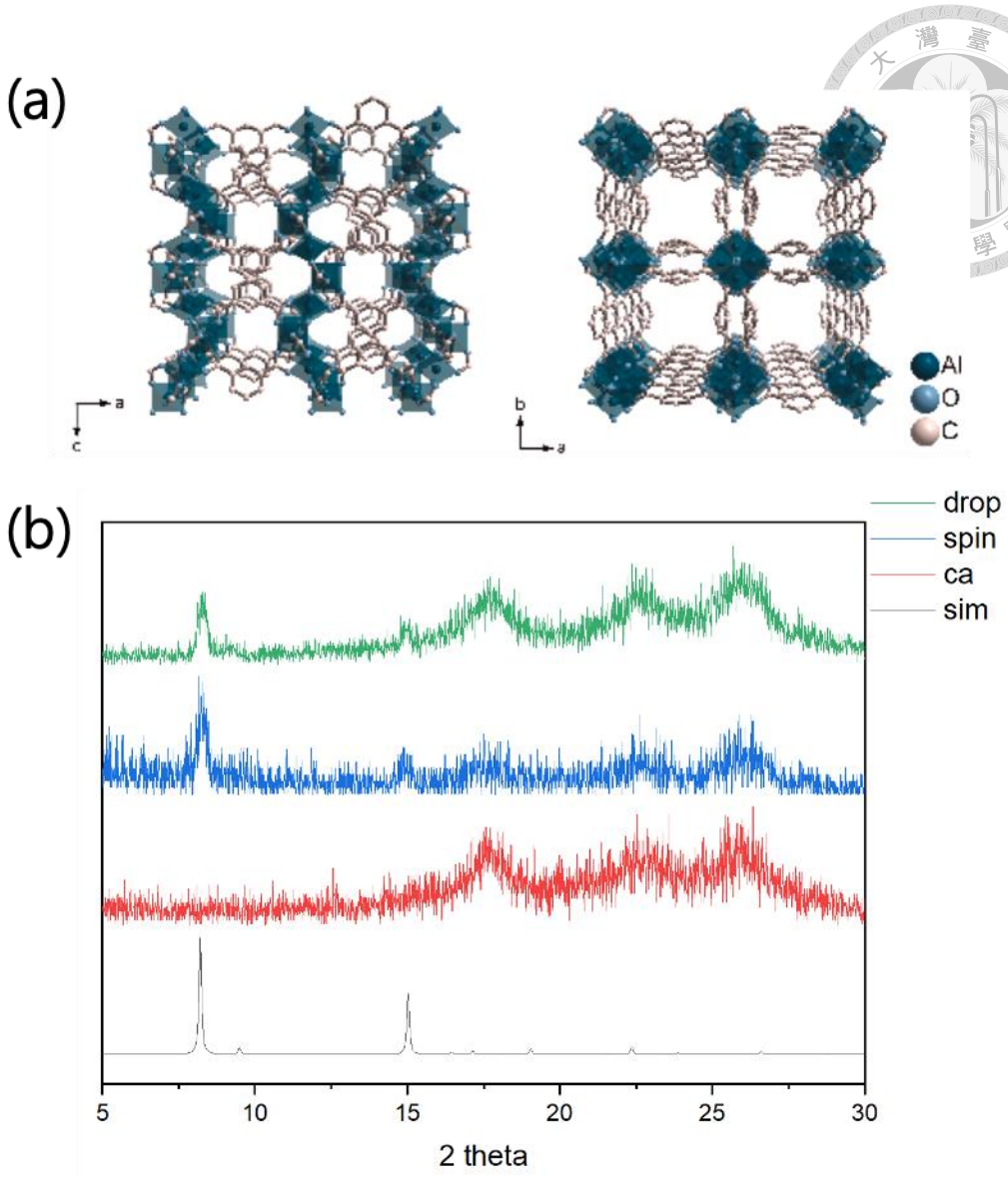

Figure 3-15. (a) Schematic illustration of the CAU-10-H crystal structure.[43] (b) XRD result of the CA substrate and the synthesized CAU-10-H membranes seeded using drop coating and spin coating methods.

Since the thickness of the CAU-10-H membrane synthesized through secondary growth was very thin, several tryouts were conducted. CAU-10-H_1.5x was grown in the secondary growth solution with 1.5 times of the reactants and the reaction time was

doi:10.6342/NTU202301269

increased by 2 hours. However, from the SEM images shown in **Figure 3-16a and b**, not only the thickness did not increase, there was too little grains to even cover the substrate, and there was nearly no grains grown in **Figure 3-16c**.

The second trial was to proceed third growth for CAU-10-H grains to grow bigger on the chance of increasing the thickness of the synthesized membrane. The seeded substrate was immersed in a secondary growth solution to react two times. The SEM result was as shown in **Figure 3-16 d** to **Figure 3-16f**. The CAU-10-H grains did grow on the substrate and were distributed uniformly. However, as shown in the cross-section SEM image (**Figure 3-16f**), the surface of the substrate was found to be destructed. The fluff-like layer disappeared with only the inner coarse fiber left. The CAU-10-H grains were grown directly onto the coarse fiber and the surface was corrugated, and the thickness of the membrane could not even be defined. The disappearance of the fluff-like layer of the CA substrate was suggested to be due to the long immersion time in the secondary growth solution of which containing dimethylformamide as part of the cosolvent so that the fluff-like layer was dissolved.

doi:10.6342/NTU202301269

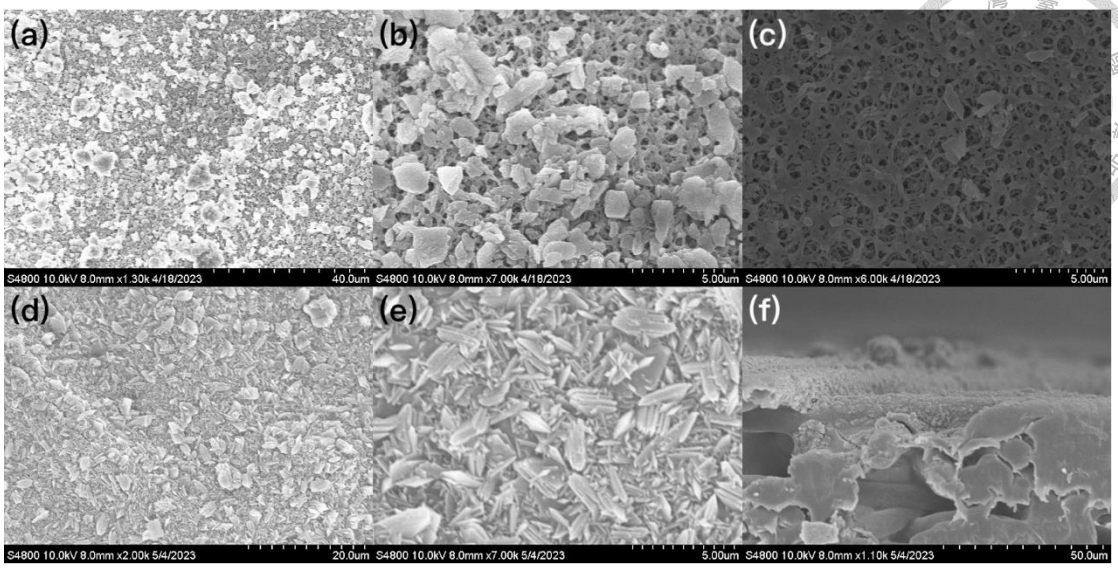

Figure 3-16. SEM images of CAU-10-H_1.5x seeded by (a,b) drop coating and (c) spin coating, (d-f) CAU-10-H_3rd.

3.2.2 Surface Characterization of Deposited Solar Absorber Layer

After tuning the growth conditions of the CAU-10-H film, solar absorber layer was further deposited onto the MOF layer. Carbon black dispersed solution was first spread-coated onto the membrane, and polydopamine was then living-polymerized onto the surface. From **Figure 3-17a and b**, a layer of solar absorber could be clearly seen in both CA_CB_PDA and CA_CAU-10-H_CB_PDA with thickness of 6.22 μm and 4.10 μm respectively. The difference between the thickness of the two deposited layers may be due to the difference of affinities between polydopamine and the adhered surfaces—polydopamine may adhere more strongly to CA membrane rather than CAU-10-H membrane. As for the top-view of the SEM images shown in **Figure 3-17c and d**, the

doi:10.6342/NTU202301269

morphologies of the two platforms looked alike. The surfaces were both covered with a uniform layer consisting of small spherical particles which were carbon black or polydopamine as these two grew into similar shapes and could not be distinguished from the SEM images, and the larger particles in the images were carbon black aggregates. Moreover, the SEM image of CA_CAU-10-H_CB_PDA after undergoing water evaporation test was also acquired to see if the platform would be destroyed in the process. From the comparison between **Figure 3-17d** and **Figure 3-17e**, there were no significant changes happened to the platform with only some cracks appeared.

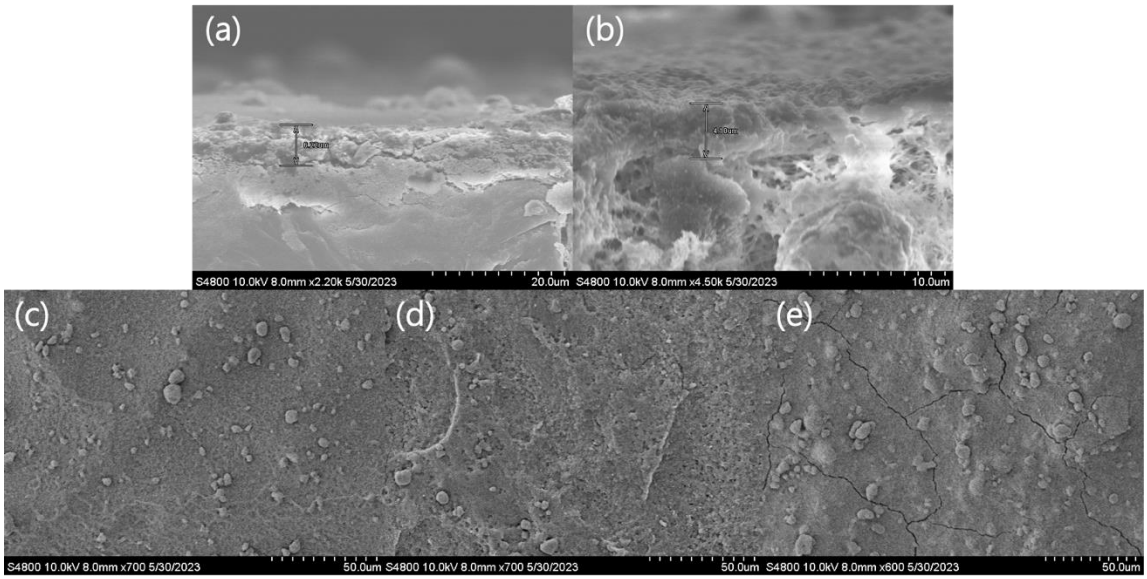

Figure 3-17. Cross-section SEM images of (a) CA_CB_PDA, (b) CA_CAU-10-H_CB_PDA. SEM images of (a) CA_CB_PDA, (b) CA_CAU-10-H_CB_PDA, (c) CA_CAU-10-H_CB_PDA after water evaporation test.

doi:10.6342/NTU202301269

3.2.3 Water Evaporation Test of Different MOF Films

Water evaporation rate of each of the membranes fabricated were tested. As shown in **Figure 2-2**, the desalination membrane was directly floating on the surface of water. The mass change, which is also the quantity of water evaporated into the air, was recorded over time as shown in **Figure 3-18**. The calculated evaporation rate and the surface temperature of the desalination membrane were recorded as listed in **Table 3-1**. According to the results, the membrane synthesized with a layer of CAU-10-H and deposited with a layer of solar absorber (CA_CAU-10-H_CB_PDA) performed the best water evaporation ability. The one performed the second highest evaporation rate was CA substrate directly coating with a layer of solar absorber (CA_CB_PDA), and the third one was CA substrate grown with third growth CAU-10-H and solar absorber (CA_CAU-10-H_3rd_CB_PDA). This result shows that the ones deposited with a solar absorber layer consisting of carbon black and polydopamine behaved better on the water evaporation test since solar absorber could help to absorb sunlight and convert it into heat, which could also be confirmed with the recorded surface temperature of the three membranes higher than the ones that did not possess solar absorber layer. The three membranes all show similar dry temperatures, which proves the deposited solar absorber layer to be stable. With similar dry temperatures, however, the water evaporation rates were not the same. Previous study[43] had shown that the thicker the MOF layer, the better the heat

doi:10.6342/NTU202301269

insulating ability, however, the water evaporation efficiency did not keep increasing with the surface temperature since a thick MOF layer also indicated that water had to transport a longer distance to reach the surface and be evaporated. As a result, there should be an optimization between surface temperature and water transportation distance to determine the best condition to have the best water evaporation ability. Here in our study, though having a lower surface temperature in dry-state rather than CA_CB_PDA, CA_CAU-10-H_CB_PDA behaved a higher surface temperature in wet-state due to the heating insulating property of CAU-10-H to prevent heat loss into bulk water. Moreover, from the comparison between CA and CA_CAU-10-H, the two membranes both without solar absorber to absorb sunlight had a similar surface temperature in dry-state and the same in wet-state, and CAU-10-H performed a better water evaporation efficiency. Therefore, the CAU-10-H layer could be confirmed to have a fast water transport ability. With insulating property to concentrate the heat and good water transport ability to pump the water to the surface, CA_CAU-10-H_CB_PDA thus performed the best evaporation efficiency. As to CA_CAU-10-H_3rd_CB_PDA, SEM images shown in previous section pointed out that the fluff-like layer on the surface of the CA substrate was destructed suggesting to be dissolved by DMF and the CAU-10-H grains were grown directly onto the left coarse fiber. With the fluff-like which is of regular porous structure being dissolved, the pores of the left coarse fiber were too large for the capillary wicking force to bring the water up to

doi:10.6342/NTU202301269

the surface. This could also be confirmed by the recorded surface temperature. The surface temperature of CA_CAU-10-H_3rd_CB_PDA in wet-state was abnormally high. This was due to little water being brought up to the surface. As a result, CA_CAU-10-H_3rd_CB_PDA behaved a poor water evaporation ability.

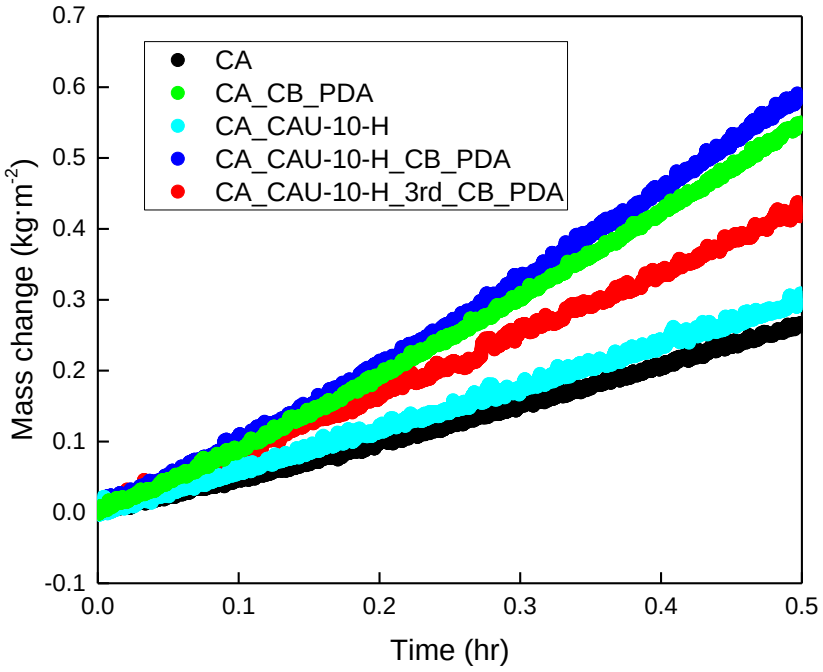

Figure 3-18. The mass change with time of different films during water evaporation test.

doi:10.6342/NTU202301269

Table 3-1. The results of the water evaporation test of different films.

Film	Evaporation rate ($kg \cdot m^{-2} \cdot h^{-1}$)		Surface temperature (℃)	
	30 min	Last 15 min	Dry (10 min)	Wet (30 min)
CA	0.5348	0.5688	33.4	32.6
CA_CB_PDA	1.1163	1.2111	86	39.2
CA_CAU-10-H	0.5963	0.6066	33	32.6
CA_CAU-10-H_CB_PDA	1.1963	1.3062	84.5	40.6
CA_CAU-10-H_3rd_CB_PDA	0.8529	0.8725	85.7	72.3

3.2.4 Cyclability Test of Water Evaporation Test

Cyclability test was further performed to test the reusability of the desalination platforms. After the first time of the water evaporation test, the platform was dried on the hot plate at 50 ℃ and stored in the humidity control box. The platform was taken out to repeat the water evaporation test twelve days later. The results were as shown in **Figure 3-19** and **Table 3-2**. For the CA_CB_PDA platform, the evaporation rate decreased on

doi:10.6342/NTU202301269

the second test, and the surface temperature also decreased. This result may be due to the destruction of the platform. The water transport path inside the membrane may be destructed and obstructed water transport. Moreover, the outside solar absorber layer may decay or easily be damaged so that the heating effect may become lower. As from the SEM images in the previous section, there were some cracks on the surface of the solar absorber layer. During operation, the cracks may become larger, and the cracks would destroy the water transport worked by capillary wicking force. Therefore, the evaporation efficiency decreased on the second test. As for the CA_CAU-10-H_3rd_CB_PDA platform, the evaporation efficiency rose on the second test. We didn't come out of any reasonable explanation to support the result. More experimental results were needed to be conducted to have a more complete understanding to conclude the cyclability property of the platforms.

doi:10.6342/NTU202301269

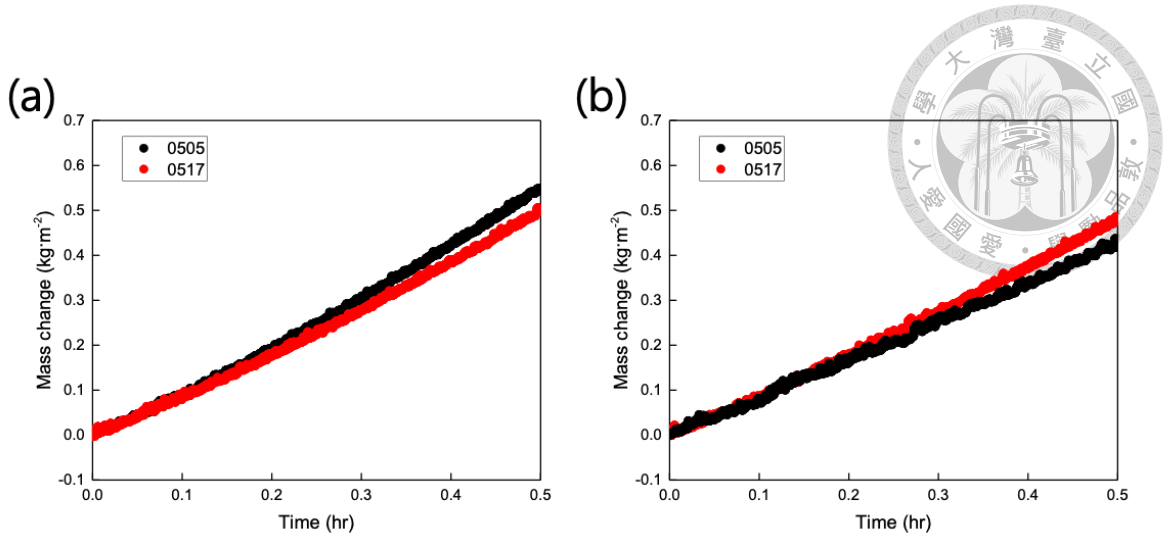

Figure 3-19. The mass change with time of (a) CA_CB_PDA and (b) CA_CAU-10-H_3rd_CB_PDA during water evaporation test with the experiments conducted using the same desalination platform and tested on different days.

Table 3-2. The water evaporation cyclability test of different films.

Film		**Evaporation rate ($kg \cdot m^{-2} \cdot h^{-1}$)**		**Surface temperature (℃)**	
		30 min	Last 15 min	Dry (10 min)	Wet (30 min)
CA_CB_PDA	5/5	1.1163	1.2111	86	39.2
	5/17	1.0168	1.1077	81.2	37.7
CA_CAU-10-H_3rd_CB_PDA	5/5	0.8529	0.8725	85.7	72.3
	5/17	0.9713	1.0292	83	70

doi:10.6342/NTU202301269

3.2.5 Grafting of Zwitterionic SBMA Polymer Brush on Cellulose Acetate Membrane

On the other hand, the grafting of zwitterionic polymer brush on CA substrate (**Figure 3-20a**) was proceeded in parallel. A two-step procedure (**Figure 3-20b**) was used to functionalize the surface of the substrate: to first anchor the bromide-functionalized initiator onto the substrate via the esterification between the bromide site and the hydroxyl groups on the cellulose acetate membrane and to start the polymerization process of the sulfobetaine methacrylate (SBMA) monomers to form zwitterionic polymer brush.

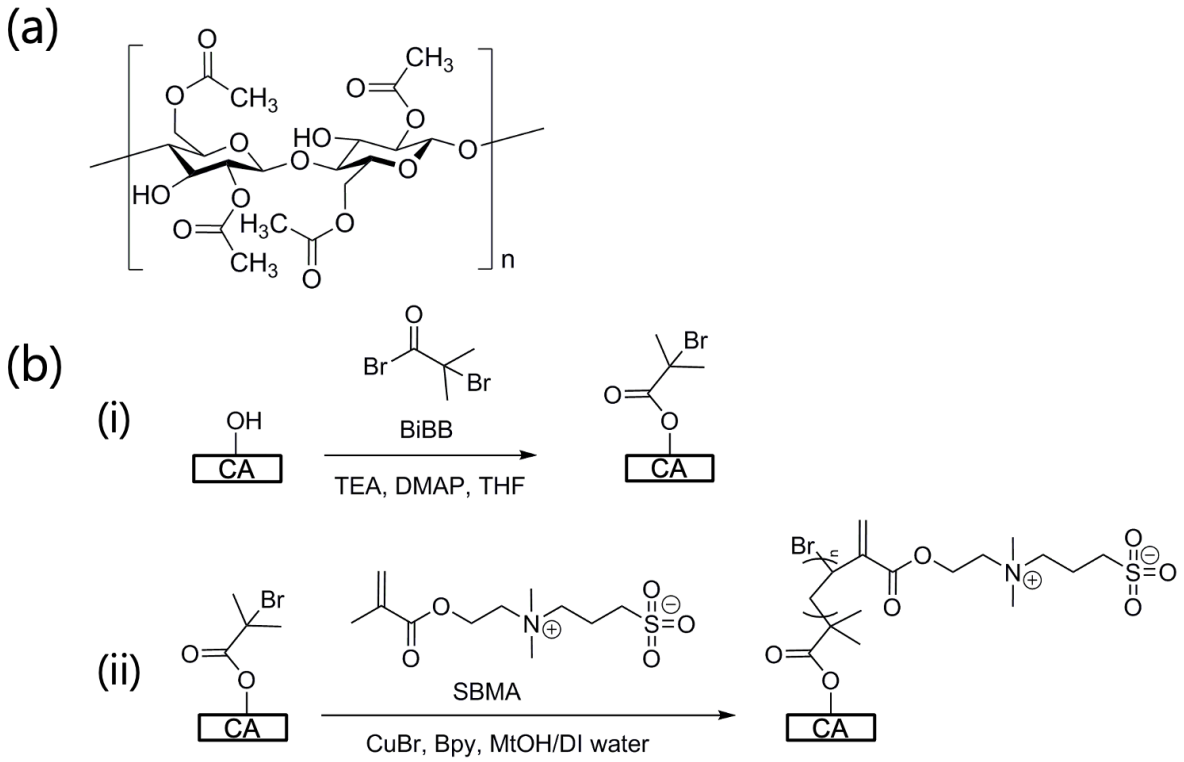

doi:10.6342/NTU202301269

Figure 3-20. Schematic illustration of (a) The chemical structure of cellulose acetate. (b) The two-step procedure to graft poly(sulfobetaine methacrylate) polymer brush onto cellulose acetate membrane filter.

3.2.6 Determination of SBMA Polymer Brush by EDS Technique

To confirm whether the initiator and the polymer brush were successfully bonded to the CA surface, first we tried to use EDS to determine the elements and the results were shown in **Figure 3-21**. Since the CA membrane was not conductive, a layer of platinum was deposited onto the sample. However, since the quantity of the target elements were too little and the signals were too weak, plus the signals of the target elements strongly overlapped with that of Pt, as a result EDS technique was not a useful tool to identify whether the initiator and the polymer brush did bind to the surface or not.

doi:10.6342/NTU202301269

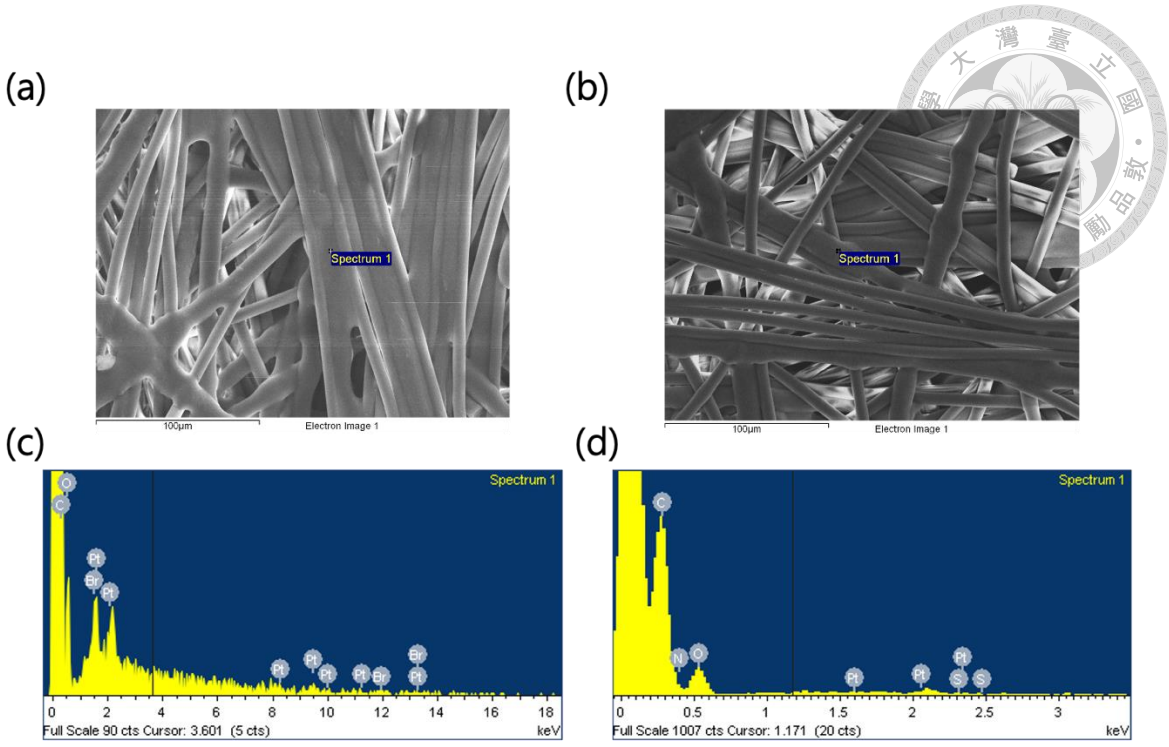

Figure 3-21. SEM images of (a) CA-Br, (b) CA-SBMA, and the EDS spectrum of (c) CA-Br, (d) CA-SBMA.

From the SEM images acquired when performing EDS (**Figure 3-21a and b**), there were something happened to the CA-SBMA film. More detailed SEM images were then obtained to know more about the surface of CA-SBMA. As shown in **Figure 3-22**, the fluff-like layer disappeared with only the inner coarse fiber left, and the polymer brush supposed to be grafted on the surface could not be observed from the SEM images. After chemical compatibility test by immersing the CA membrane filter in THF, which is the solvent used in the process of initiator immobilization, the membrane (CA_THF) was found to turn from solid white into transparent to some extent. Linking with the

doi:10.6342/NTU202301269

disappearance of the regular pore structure on the surface of the CA membrane, it could be concluded that the disappeared structure was dissolved by THF.

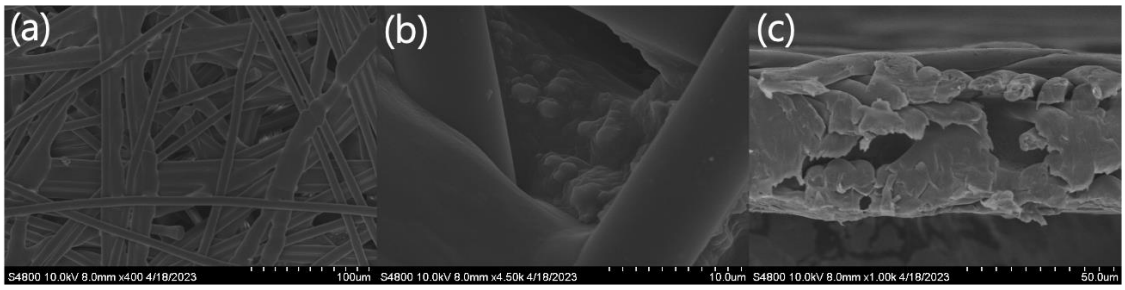

Figure 3-22. SEM images of CA substrate grafted with SBMA polymer brush.

3.2.7 Determination of SBMA Polymer Brush by XPS Technique

The chemical compositions of the modified CA surfaces were then determined using the XPS technique. As shown in **Figure 3-23**, four XPS spectra of different membranes were acquired. Starting from **Figure 3-23a**, there were two strong peaks at around 284 eV and 530 eV referring to C_{1s} and $O_{1s,}$ respectively. Originally, the ready-made cellulose acetate membrane filter was supposed only to be composed of C and H. However, there was a peak at about 402 eV, showing the N_{1s} signal. The existence of N may be due to the remains when manufacturing the CA membrane filter. The second sample was CA_THF, which had been confirmed by the SEM images that THF would dissolve the outer structures of the CA membrane. CA_THF was still composed of C and H with a signal of N remaining from the manufacturing process, but the C/O atomic concentration ratio

doi:10.6342/NTU202301269

changed and the N atomic concentration percentage decreased. The C/O ratio turned from about 0.8 of CA into about 1.53 of CA_THF, and the atomic percentage of N decreased from 9.90% to 4.11%. These atomic concentration changes may be related to the dissolved surface layer. As for the third sample CA-Br, despite the C_{1s}, O_{1s}, and N_{1s} signals of the CA substrate, there was also a weak peak at about 70 eV showing the Br_{3d} signal, and the atomic percentage of Br was 0.35%. An enlarged Br_{3d} narrow-scan spectrum was shown in **Figure 3-23c**, and the existence of the Br_{3d} signal indicated the successful immobilization of the bromide-functionalized initiator onto the CA substrate. Regarding the last sample CA-SBMA, C_{1s} and O_{1s} signals of the CA substrate were still the two strongest peaks. The targeting SBMA had two elements besides C and O: N and S. However, since there was remaining N when manufacturing the CA membrane filter, the existence of the N_{1s} signal could not be deemed as an indicator for the successful grafting of SBMA. Luckily, there was a characteristic peak at about 167 eV that could be referred to S_{2p} signal, hence confirming the successful grafting of zwitterionic SBMA polymer brush onto the CA membrane. Moreover, the absence of the Br signal suggested that the Br sites were predominantly covered by polymer brushes.

doi:10.6342/NTU202301269

(a)

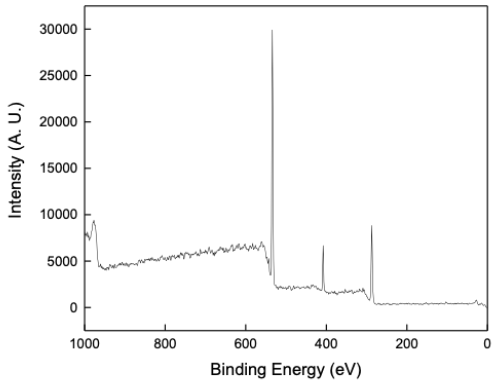

Atomic Concentration Table

C1s	N1s	O1s
0.314	0.499	0.733
5.784	9.513	14.506
40.12	9.90	49.98

(b)

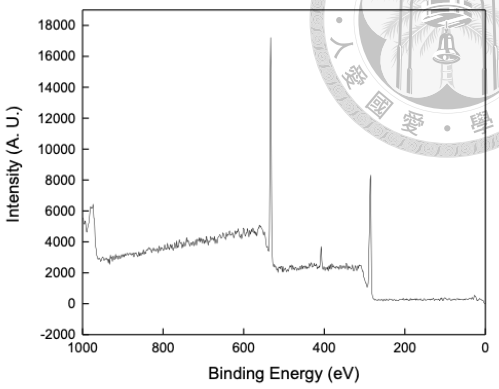

Atomic Concentration Table

C1s	N1s	O1s
0.314	0.499	0.733
5.784	9.513	14.506
58.02	4.11	37.87

(c)

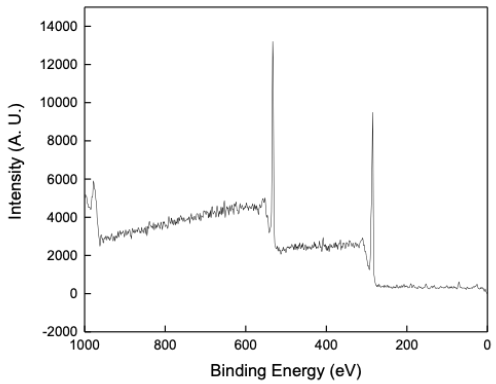

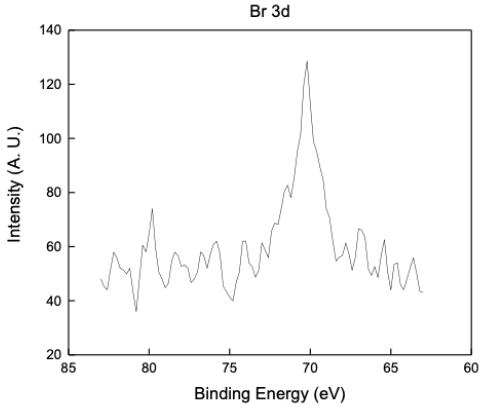

Atomic Concentration Table

C1s	N1s	O1s	Br3d
0.314	0.499	0.733	1.149
5.784	9.513	14.506	22.875
66.71	1.51	31.42	0.35

(d)

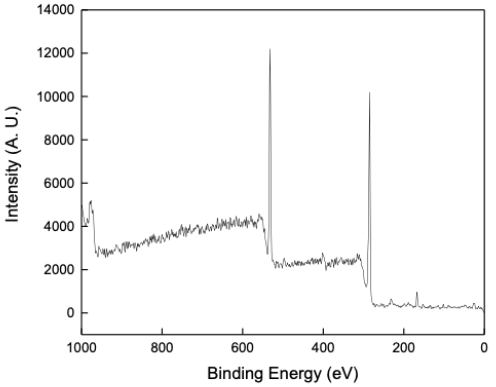

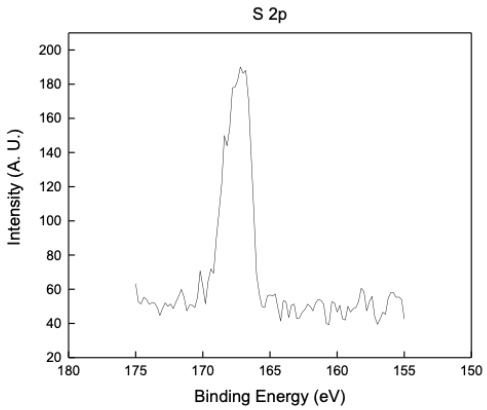

Atomic Concentration Table

C1s	N1s	O1s	S2p	Br3d
0.314	0.499	0.733	0.717	1.149
5.784	9.513	14.506	14.548	22.875
67.30	2.06	29.21	1.43	0.00

doi:10.6342/NTU202301269

Figure 3-23. XPS spectra of (a) ready-made cellulose acetate membrane filter, (b) CA membrane after 24 hours of immersion in THF (CA_THF), (c) initiator-functionalized CA membrane (CA-Br) with Br_{3d} narrow-scan spectrum, (d) zwitterionic SBMA brush-grafted CA membrane (CA-SBMA) with P_{2p} narrow-scan spectrum.

3.2.8 Water Evaporation Test of Cellulose Acetate Membrane Grafted with SBMA Polymer Brush

The water evaporation rate of CA substrate grafted with SBMA polymer brush (CA-SBMA) and CA_THF were tested. The results were as shown in **Figure 3-24** and **Table 3-3**. From the results, the water evaporation efficiency of CA_THF was the lowest, and CA-SBMA behaved a better water evaporation efficiency but still lower than that of CA membrane. According to previous SEM images of CA-SBMA film as shown in **Figure 3-22**, the surface of the film was only coarse fiber left with the regular pore structure on the CA surface being dissolved by THF solvent confirmed by the chemical compatibility test of CA_THF. Therefore, the poor behavior of the films may be due to the regular porous structure being dissolved, and the pores of the left coarse fiber were too large for the capillary wicking force to bring the water up to the surface. The water transport ability decreased so that the evaporation efficiency decreased. This may also be confirmed by

doi:10.6342/NTU202301269

the higher wet-state surface temperatures of CA_THF and CA-SBMA than the CA membrane. In addition, the CA-SBMA film behaved better water evaporation efficiency than CA_THF. This may be due to the effect of the zwitterionic polymer brush grafting on the bottom of the substrate. The mechanism was remained to be verified by further investigations.

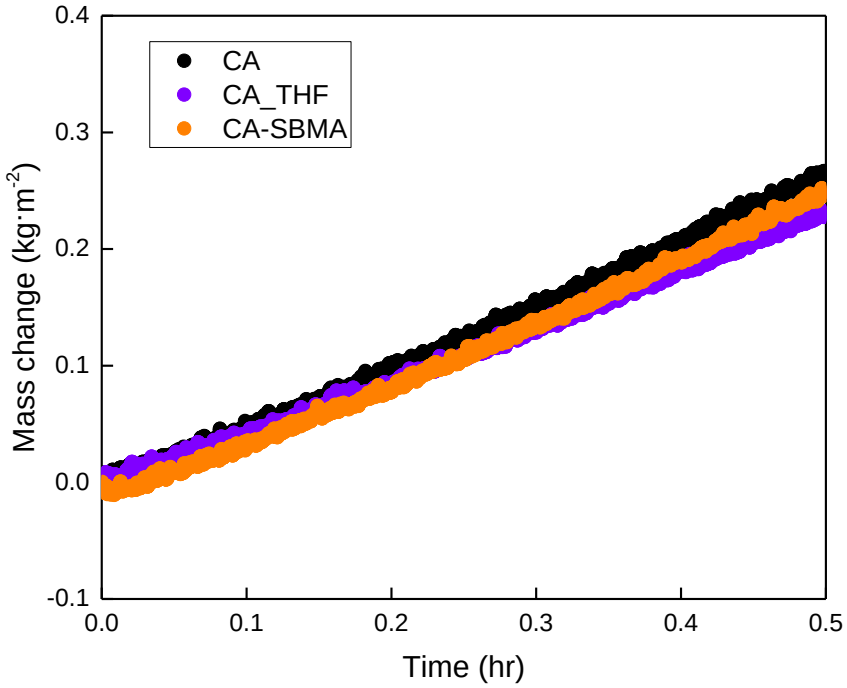

Figure 3-24. The mass change with time of cellulose acetate grafted with SBMA polymer brush during water evaporation test.

doi:10.6342/NTU202301269

Table 3-3. The results of the water evaporation test of cellulose acetate grafted with SBMA polymer brush.

Film	Evaporation rate ($kg \cdot m^{-2} \cdot h^{-1}$)		Surface temperature (℃)	
	30 min	Last 15 min	Dry (10 min)	Wet (30 min)
CA	0.5348	0.5688	33.4	32.6
CA_THF	0.4679	0.5014	35.9	34.9
CA-SBMA	0.5271	0.5651	36	35

doi:10.6342/NTU202301269

Chapter 4 Conclusion

4.1 Surface Charge Tuning of Poly(EDOT-N^+-*co*-EDOT-COOH)

In this study, we synthesized new positively charged EDOT-N^+ monomers. Using co-electropolymerization with EDOT-COOH, we successfully synthesized poly(EDOT-N^+-*co*-EDOT-COOH) with different surface charges. The surface properties have been investigated by using AFM and contact angle. Besides, we applied TBO staining to calculate the ratio of EDOT-N^+ and EDOT-COOH in the copolymers. We then used QCM to study the adsorption of BSA and LYZ on poly(EDOT-N^+-*co*-EDOT-COOH) compared to poly(EDOT-N^+) and poly(EDOT-COOH). Based on the results, we can conclude that the mechanism of BSA and LYZ adsorption on poly(EDOT-N^+-*co*-EDOT-COOH) is summarized in **Figure 4-1**. The adsorption is mainly controlled by the electrostatic force between proteins and surface charge. Although the BSA is negatively charged, the recognition with COOH groups dominates the binding behavior on a negatively charged poly(EDOT-N^+-*co*-EDOT-COOH). Despite the electrostatic force between the two kinds of proteins and the charged poly(EDOT-COOH) and poly(EDOT-N^+), the adsorption behavior of both BSA and LYZ on poly(EDOT-N^+-*co*-EDOT-COOH) of different compositions both showed the good antifouling property at [EDOT-N^+] : [EDOT-COOH] = 8 : 2 in which we considered to be at real 1:1 ratio of the copolymer, creating a

doi:10.6342/NTU202301269

zwitterion-like poly(EDOT-N$^+$-*co*-EDOT-COOH) copolymer.

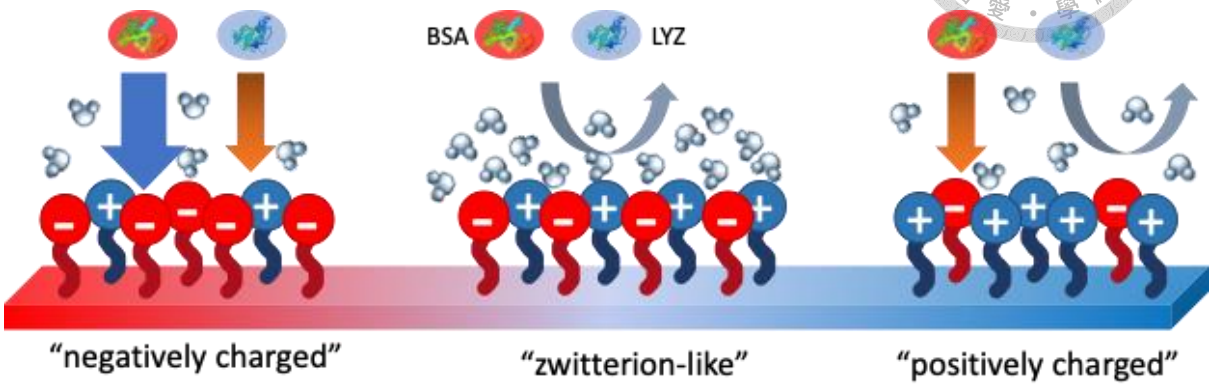

Figure 4-1. The schematic illustration of BSA and LYZ adsorption behavior on poly(EDOT-N$^+$-*co*-EDOT-COOH) when the surface charge is manipulated.[47]

4.2 Zwitterionic Polymer Brush-Modified Metal-Organic Framework-Based Solar Desalination Platform

In this study, the experiments were divided into two parts. In the first part, we successfully synthesized CAU-10-H membrane on the CA substrate, and then deposited a layer of solar absorber composed of carbon black and polydopamine. The platforms were then tested for their water evaporation rate. The solar absorber layer deposited was verified to help absorb light and convert into heat, making the surface temperature increased substantially, and the CAU-10-H MOF layer was proved to increase the water transport ability and help to prevent heat loss away from the top of the surface. Among

doi:10.6342/NTU202301269

all the platforms made with different fabrication parameters, CA_CAU-10-H_CB_PDA performed the best water evaporation efficiency. The second part was the grafting of zwitterionic polymer brush onto the CA substrate. A two-step procedure was used to first immobilize bromide-functionalized initiator onto the CA surface and then undergo living polymerization to form the poly(sulfobetaine methacrylate) polymer brush. Both of the two steps were confirmed by XPS technique to successfully bind the targeting molecules.

doi:10.6342/NTU202301269

Chapter 5 Future Work

5.1 Surface Charge Tuning of Poly(EDOT-N^+-*co*-EDOT-COOH)

The special dissipation change when proteins bound to the poly(EDOT-COOH) surface remains an interesting question. Further studies should be conducted to understand the hydration status change happened on the poly(EDOT-N^+-*co*-EDOT-COOH) surface.

Moreover, in addition to the fact that at a feed ratio of [EDOT-N^+] : [EDOT-COOH] = 8 : 2 in which an actual 1:1 ratio was realized and that at this composition the poly(EDOT-N^+-*co*-EDOT-COOH) film performed good antifouling property, further studies should be carried out to look into the distribution of the two kinds of monomers in this copolymer. Were they in the form of random copolymer or block copolymer? Would there be clusters of poly(EDOT-N^+) and poly(EDOT-COOH) or they were just randomly distributed? Deeper investigations into the orders of monomers would give more valid clues about the zwitterion-like phenomenon.

5.2 Zwitterionic Polymer Brush-Modified Metal-Organic Framework-Based Solar Desalination Platform

Though successfully grew the MOF layer and grafted the zwitterionic polymer brush

doi:10.6342/NTU202301269

onto the substrate, some problems remained to be solved. The first one is that the CA membrane filter substrate would be dissolved by DMF and THF with both of the solvents necessary in the fabrication process. The second one is that the CA substrate could not float on the liquid surface, so during the process of the grafting of the polymer brush, the CA membrane filter would sink into the reacted solution and the polymer brush would grow on both sides of the CA membrane. Moreover, when depositing the solar absorber layer, the CA membrane was also sunk into the reacted solution and there were little polydopamine would grow on the bottom of the CA membrane. As a result, to grow MOF layer and solar absorber layer first or to grow polymer brush first remained a question.

In future work, we planned to change the substrate from cellulose acetate to glass fiber membrane filter which is chemically compatible with the reacted solvents. Different fabrication conditions of growing MOF membrane should be tried out to optimize between the heat insulating property of MOF and the water transport ability. Zwitterionic polymer brush was planned to be grafted onto the glass fiber substrate through silane chemistry. Further antifouling tests would be conducted by fluorescent protein adhesion test, and the adhesion tests of other common pollutants like oil and organic dyes.

doi:10.6342/NTU202301269

REFERENCE

(1) Guo, X.; Facchetti, A. The Journey of Conducting Polymers from Discovery to Application. *Nat. Mater.* **2020**, *19* (9), 922-928.

(2) Rivnay, J.; Owens, R. M.; Malliaras, G. G. The Rise of Organic Bioelectronics. *Chem. Mater.* **2013**, *26* (1), 679-685.

(3) Simon, D. T.; Gabrielsson, E. O.; Tybrandt, K.; Berggren, M. Organic Bioelectronics: Bridging the Signaling Gap between Biology and Technology. *Chem. Rev.* **2016**, *116* (21), 13009-13041.

(4) Guimard, N. K.; Gomez, N.; Schmidt, C. E. Conducting Polymers in Biomedical Engineering. *Prog. Polym. Sci.* **2007**, *32* (8-9), 876-921.

(5) Luo, S.-C. Conducting Polymers as Biointerfaces and Biomaterials: A Perspective for a Special Issue of Polymer Reviews. *Polym. Rev.* **2013**, *53* (3), 303-310.

(6) Peng, Y.; Pi, M.; Zhang, X.; Yan, B.; Li, Y.; Shi, L.; Ran, R. High Strength, Antifreeze, and Moisturizing Conductive Hydrogel for Human-motion Detection. *Polymer* **2020**, *196*.

(7) Choi, J. S.; Park, J. S.; Kim, B.; Lee, B.-T.; Yim, J.-H. In Vitro Biocompatibility of Vapour Phase Polymerised Conductive Scaffolds for Cell Lines. *Polymer* **2017**, *124*, 95-100.

(8) Zhu, B.; Luo, S. C.; Zhao, H.; Lin, H. A.; Sekine, J.; Nakao, A.; Chen, C.; Yamashita, Y.; Yu, H. H. Large Enhancement in Neurite Outgrowth on a Cell Membrane-Mimicking Conducting Polymer. *Nat. Commun.* **2014**, *5*, 4523.

(9) Chin, M.; Tada, S.; Tsai, M. H.; Ito, Y.; Luo, S. C. Strategy to Immobilize Peptide Probe Selected through In Vitro Ribosome Display for Electrochemical Aptasensor Application. *Anal. Chem.* **2020**, *92* (16), 11260-11267.

doi:10.6342/NTU202301269

(10) Pitsalidis, C.; Pappa, A. M.; Boys, A. J.; Fu, Y.; Moysidou, C. M.; van Niekerk, D.; Saez, J.; Savva, A.; Iandolo, D.; Owens, R. M. Organic Bioelectronics for In Vitro Systems. *Chem. Rev.* **2022**, *122* (4), 4700-4790.

(11) Berggren, M.; Glowacki, E. D.; Simon, D. T.; Stavrinidou, E.; Tybrandt, K. In Vivo Organic Bioelectronics for Neuromodulation. *Chem. Rev.* **2022**, *122* (4), 4826-4846.

(12) Hsiao, Y. S.; Liao, Y. H.; Chen, H. L.; Chen, P.; Chen, F. C. Organic Photovoltaics and Bioelectrodes Providing Electrical Stimulation for PC12 Cell Differentiation and Neurite Outgrowth. *ACS Appl. Mater. Interfaces* **2016**, *8* (14), 9275-9284.

(13) Aerathupalathu Janardhanan, J.; Chen, Y. L.; Liu, C. T.; Tseng, H. S.; Wu, P. I.; She, J. W.; Hsiao, Y. S.; Yu, H. H. Sensitive Detection of Sweat Cortisol Using an Organic Electrochemical Transistor Featuring Nanostructured Poly(3,4-Ethylenedioxythiophene) Derivatives in the Channel Layer. *Anal. Chem.* **2022**, *94* (21), 7584-7593.

(14) Lin, H. A.; Zhu, B.; Wu, Y. W.; Sekine, J.; Nakao, A.; Luo, S. C.; Yamashita, Y.; Yu, H. H. Dynamic Poly(3,4-ethylenedioxythiophene)s Integrate Low Impedance with Redox-Switchable Biofunction. *Adv. Funct. Mater.* **2018**, *28* (12).

(15) Ludwig, K. A.; Uram, J. D.; Yang, J.; Martin, D. C.; Kipke, D. R. Chronic Neural Recordings Using Silicon Microelectrode Arrays Electrochemically Deposited with a Poly(3,4-ethylenedioxythiophene) (PEDOT) Film. *J. Neural Eng.* **2006**, *3* (1), 59-70.

(16) Cui, X.; Martin, D. C. Electrochemical Deposition and Characterization of Poly(3,4-ethylenedioxythiophene) on Neural Microelectrode Arrays. *Sens. Actuators, B* **2003**, *89* (1), 92-102.

(17) Bodart, C.; Rossetti, N.; Hagler, J. E.; Chevreau, P.; Chhin, D.; Soavi, F.;

doi:10.6342/NTU202301269

Schougaard, S. B.; Amzica, F.; Cicoira, F. Electropolymerized Poly(3,4-ethylenedioxythiophene) (PEDOT) Coatings for Implantable Deep-Brain-Stimulating Microelectrodes. *ACS Appl. Mater. Interfaces* **2019**, *11* (19), 17226-17233.

(18) Ludwig, K. A.; Langhals, N. B.; Joseph, M. D.; Richardson-Burns, S. M.; Hendricks, J. L.; Kipke, D. R. Poly(3,4-ethylenedioxythiophene) (PEDOT) Polymer Coatings Facilitate Smaller Neural Recording Electrodes. *J. Neural Eng.* **2011**, *8* (1), 014001.

(19) Wilks, S.; Richardson-Burn, S.; Hendricks, J.; Martin, D.; Otto, K. Poly(3,4-ethylenedioxythiophene) (PEDOT) as a Micro-Neural Interface Material for Electrostimulation. *Front. Neuroeng.* **2009**, *2*, Original Research.

(20) Wu, J. G.; Chen, J. H.; Liu, K. T.; Luo, S. C. Engineering Antifouling Conducting Polymers for Modern Biomedical Applications. *ACS Appl. Mater. Interfaces* **2019**, *11* (24), 21294-21307.

(21) Wang, Y. S.; Yau, S.; Chau, L. K.; Mohamed, A.; Huang, C. J. Functional Biointerfaces Based on Mixed Zwitterionic Self-Assembled Monolayers for Biosensing Applications. *Langmuir* **2019**, *35* (5), 1652-1661.

(22) Chen, S.; Li, L.; Zhao, C.; Zheng, J. Surface Hydration: Principles and Applications toward Low-Fouling/Nonfouling Biomaterials. *Polymer* **2010**, *51* (23), 5283-5293.

(23) Chen, Y.; Luo, S. C. Synergistic Effects of Ions and Surface Potentials on Antifouling Poly(3,4-ethylenedioxythiophene): Comparison of Oligo(Ethylene Glycol) and Phosphorylcholine. *Langmuir* **2019**, *35* (5), 1199-1210.

(24) Shimizu, A.; Hifumi, E.; Kojio, K.; Takahara, A.; Higaki, Y. Modulation of Double Zwitterionic Block Copolymer Aggregates by Zwitterion-Specific

doi:10.6342/NTU202301269

Interactions. *Langmuir* **2021**, *37* (50), 14760-14766.

(25) Fan, Y. J.; Pham, M. T.; Huang, C. J. Development of Antimicrobial and Antifouling Universal Coating via Rapid Deposition of Polydopamine and Zwitterionization. *Langmuir* **2019**, *35* (5), 1642-1651.

(26) Ma, N.; Cao, J.; Li, H.; Zhang, Y.; Wang, H.; Meng, J. Surface Grafting of Zwitterionic and PEGylated Cross-Linked Polymers toward PVDF Membranes with Ultralow Protein Adsorption. *Polymer* **2019**, *167*, 1-12.

(27) Huang, J. J.; Lin, C. H.; Tanaka, Y.; Yamamoto, A.; Luo, S. C.; Tanaka, M. Manipulation of Surface Hydration States by Tuning the Oligo(Ethylene Glycol) Moieties on PEDOT to Achieve Platelet-Resistant Bioelectrode Applications. *Adv. Mater. Interfaces* **2022**.

(28) Mukai, M.; Cheng, C. H.; Ma, W.; Chin, M.; Lin, C. H.; Luo, S. C.; Takahara, A. Synthesis of a Conductive Polymer Thin Film Having a Choline Phosphate Side Group and its Bioadhesive Properties. *Chem Commun (Camb)* **2020**, *56* (18), 2691-2694.

(29) Lin, C. H.; Luo, S. C. Combination of AFM and Electrochemical QCM-D for Probing Zwitterionic Polymer Brushes in Water: Visualization of Ionic Strength and Surface Potential Effects. *Langmuir* **2021**, *37* (42), 12476-12486.

(30) Fujii, S.; Kozuka, S.; Yokota, K.; Ishihara, K.; Yusa, S. I. Preparation of Biocompatible Poly(2-(methacryloyloxy)ethyl phosphorylcholine) Hollow Particles Using Silica Particles as a Template. *Langmuir* **2022**, *38* (18), 5812-5819.

(31) Sakamaki, T.; Inutsuka, Y.; Igata, K.; Higaki, K.; Yamada, N. L.; Higaki, Y.; Takahara, A. Ion-Specific Hydration States of Zwitterionic Poly(sulfobetaine methacrylate) Brushes in Aqueous Solutions. *Langmuir* **2019**, *35* (5), 1583-1589.

doi:10.6342/NTU202301269

(32) Higaki, Y.; Inutsuka, Y.; Sakamaki, T.; Terayama, Y.; Takenaka, A.; Higaki, K.; Yamada, N. L.; Moriwaki, T.; Ikemoto, Y.; Takahara, A. Effect of Charged Group Spacer Length on Hydration State in Zwitterionic Poly(sulfobetaine) Brushes. *Langmuir* **2017**, *33* (34), 8404-8412.

(33) Lin, C. H.; Luo, S. C. Zwitterionic Conducting Polymers: From Molecular Design, Surface Modification, and Interfacial Phenomenon to Biomedical Applications. *Langmuir* **2022**, *38* (24), 7383-7399.

(34) Erfani, A.; Seaberg, J.; Aichele, C. P.; Ramsey, J. D. Interactions between Biomolecules and Zwitterionic Moieties: A Review. *Biomacromolecules* **2020**, *21* (7), 2557-2573.

(35) Zhao, F.; Guo, Y.; Zhou, X.; Shi, W.; Yu, G. Materials for Solar-Powered Water Evaporation. *Nat. Rev. Mater.* **2020**, *5* (5), 388-401.

(36) Chen, C.; Kuang, Y.; Hu, L. Challenges and Opportunities for Solar Evaporation. *Joule* **2019**, *3* (3), 683-718.

(37) Li, Z.; Wang, C.; Su, J.; Ling, S.; Wang, W.; An, M. Fast-Growing Field of Interfacial Solar Steam Generation: Evolutional Materials, Engineered Architectures, and Synergistic Applications. *Solar RRL* **2019**, *3* (3), 1800206.

(38) Liu, X.; Mishra, D. D.; Wang, X.; Peng, H.; Hu, C. Towards Highly Efficient Solar-Driven Interfacial Evaporation for Desalination. *J. Mater. Chem. A* **2020**, *8* (35), 17907-17937, 10.1039/C9TA12612K.

(39) Zhou, H.-C.; Long, J. R.; Yaghi, O. M. Introduction to Metal–Organic Frameworks. *Chem. Rev.* **2012**, *112* (2), 673-674.

(40) Furukawa, H.; Cordova, K. E.; O'Keeffe, M.; Yaghi, O. M. The Chemistry and Applications of Metal-Organic Frameworks. *Science* **2013**, *341* (6149), 1230444.

(41) Abdullah, N.; Yusof, N.; Ismail, A. F.; Lau, W. J. Insights into Metal-Organic

doi:10.6342/NTU202301269

Frameworks-Integrated Membranes for Desalination Process: A Review. *Desalination* **2021**, *500*, 114867.

(42) Cao, Z.; Liu, V.; Barati Farimani, A. Water Desalination with Two-Dimensional Metal–Organic Framework Membranes. *Nano Lett.* **2019**, *19* (12), 8638-8643.

(43) Hu, T.-N.; Hsu, C.-H.; Chiou, D.-S.; Kang, D.-Y.; Luo, S.-C. CAU-10-H as Efficient Water Sorbent for Solar Steam Generation. *J. Taiwan Inst. Chem. Eng.* **2022**, *141*, 104593.

(44) Liu, P.; Chen, Q.; Li, L.; Lin, S.; Shen, J. Anti-biofouling Ability and Cytocompatibility of the Zwitterionic Brushes-Modified Cellulose Membrane. *J. Mater. Chem. B* **2014**, *2* (41), 7222-7231.

(45) Xu, X.; Guillomaitre, N.; Christie, K. S. S.; Bay, R. K. n.; Bizmark, N.; Datta, S. S.; Ren, Z. J.; Priestley, R. D. Quick-Release Antifouling Hydrogels for Solar-Driven Water Purification. *ACS Cent. Sci.* **2023**, *9* (2), 177-185.

(46) Zhang, Y. Q.; Lin, H. A.; Pan, Q. C.; Qian, S. H.; Zhang, S. H.; Qiu, G.; Luo, S. C.; Yu, H. H.; Zhu, B. Tunable Protein/Cell Binding and Interaction with Neurite Outgrowth of Low-Impedance Zwitterionic PEDOTs. *ACS Appl. Mater. Interfaces* **2020**, *12* (10), 12362-12372.

(47) Lin, T.-Y.; Lo, W.-Y.; Kao, T.-Y.; Lin, C.-H.; Wu, Y.-K.; Luo, S.-C. Manipulating the Distribution of Surface Charge of PEDOT toward Zwitterion-Like Antifouling Properties. *Polymer* **2022**, *262*, 125507.

(48) Ghasemi, H.; Ni, G.; Marconnet, A. M.; Loomis, J.; Yerci, S.; Miljkovic, N.; Chen, G. Solar Steam Generation by Heat Localization. *Nat. Commun.* **2014**, *5* (1), 4449.

(49) Dao, V.-D.; Choi, H.-S. Carbon-Based Sunlight Absorbers in Solar-Driven Steam Generation Devices. *Global Challenges* **2018**, *2* (2), 1700094.

(50) Han, D.; Meng, Z.; Wu, D.; Zhang, C.; Zhu, H. Thermal Properties of Carbon

doi:10.6342/NTU202301269

Black Aqueous Nanofluids for Solar Absorption. *Nanoscale Res. Lett.* **2011**, *6* (1), 457.

(51) Zou, Y.; Yang, P.; Yang, L.; Li, N.; Duan, G.; Liu, X.; Li, Y. Boosting Solar Steam Generation by Photothermal Enhanced Polydopamine/Wood Composites. *Polymer* **2021**, *217*, 123464.

(52) Hauser, D.; Steinmetz, L.; Balog, S.; Taladriz-Blanco, P.; Septiadi, D.; Wilts, B. D.; Petri-Fink, A.; Rothen-Rutishauser, B. Polydopamine Nanoparticle Doped Nanofluid for Solar Thermal Energy Collector Efficiency Increase. *Adv. Sustainable Syst.* **2020**, *4* (1), 1900101.

(53) Wu, J. G.; Lee, C. Y.; Wu, S. S.; Luo, S. C. Ionic Liquid-Assisted Electropolymerization for Lithographical Perfluorocarbon Deposition and Hydrophobic Patterning. *ACS Appl. Mater. Interfaces* **2016**, *8* (34), 22688-22695.

(54) Liu, Y.; He, T.; Gao, C. Surface Modification of Poly(ethylene terephthalate) via Hydrolysis and Layer-by-layer Assembly of Chitosan and Chondroitin Sulfate to Construct Cytocompatible Layer for Human Endothelial Cells. *Colloids Surf., B* **2005**, *46* (2), 117-126.

(55) Luo, S.-C.; Mohamed Ali, E.; Tansil, N. C.; Yu, H.-h.; Gao, S.; Kantchev, E. A. B.; Ying, J. Y. Poly(3,4-ethylenedioxythiophene) (PEDOT) Nanobiointerfaces: Thin, Ultrasmooth, and Functionalized PEDOT Films with in Vitro and in Vivo Biocompatibility. *Langmuir* **2008**, *24* (15), 8071-8077.

(56) Xu, C.; Jiang, J.; Oguzlu, H.; Zheng, Y.; Jiang, F. Antifouling, Antibacterial and Non-Cytotoxic Transparent Cellulose Membrane with Grafted Zwitterion and Quaternary Ammonium Copolymers. *Carbohydr. Polym.* **2020**, *250*, 116960.

(57) Dixon, M. C. Quartz Crystal Microbalance with Dissipation Monitoring: Enabling Real-Time Characterization of Biological Materials and their Interactions. *J*

doi:10.6342/NTU202301269

Biomol Tech. **2008**, *19* (3), 151-158.

(58) Easley, A. D.; Ma, T.; Eneh, C. I.; Yun, J.; Thakur, R. M.; Lutkenhaus, J. L. A Practical Guide to Quartz Crystal Microbalance with Dissipation Monitoring of Thin Polymer Films. *J. Polym. Sci.* **2022**, *60* (7), 1090-1107.

(59) Shyh-Chyang Luo, E. M. A., Natalia C. Tansil, Hsiao-hua Yu, Shujun Gao, Eric A. B. Kantchev, and Jackie Y. Ying. Poly(3,4-ethylenedioxythiophene) (PEDOT) Nanobiointerfaces: Thin, Ultrasmooth, and Functionalized PEDOT Films with in Vitro and in Vivo Biocompatibility. *Langmuir* **2008**, *24*, 6.

(60) Chau, T. T.; Bruckard, W. J.; Koh, P. T.; Nguyen, A. V. A Review of Factors that Affect Contact Angle and Implications for Flotation Practice. *Adv. Colloid Interface Sci.* **2009**, *150* (2), 106-115.

(61) Kanazawa, K. K.; Gordon, J. G. Frequency of a Quartz Microbalance in Contact with Liquid. *Anal. Chem.* **1985**, *57* (8), 1770-1771. DOI: 10.1021/ac00285a062.

(62) Sauerbrey, G. Verwendung von Schwingquarzen zur Wägung dünner Schichten und zur Mikrowägung. *Zeitschrift für Physik* **1959**, *155* (2), 206-222.

(63) Parks, J. S.; Cistola, D. P.; Small, D. M.; Hamilton, J. A. Interactions of the Carboxyl Group of Oleic Acid with Bovine Serum Albumin: A 13C NMR Study. *J. Biol. Chem.* **1983**, *258* (15), 9262-9269.

(64) Moriguchi, I. Protein Bindings. II. Binding of Aromatic Carboxylic Acids to Bovine Serum Albumin. *Chem. Pharm. Bull.* **1968**, *16* (4), 597-600.

doi:10.6342/NTU202301269